Small

NANO · MICRO small
www.small-journal.com

RESEARCH ARTICLE OPEN ACCESS

Ligand-Driven Optimization of Iron Oxide Nanoprobes for In Vivo MRI Enhancement at Ultra-High Field

Pelayo García-Acevedo[1,2,3] | María Luz Alonso-Alonso[2] | Sara Ortega-Espina[2] | Manuel Bañobre-López[3] | Yolanda Piñeiro[1] | Ramón Iglesias-Rey[2] | José Rivas[1]

[1]NANOMAG Laboratory, Applied Physics Department, iMATUS Materials Institute and Health Research Institute of Santiago de Compostela (IDIS), Universidade de Santiago de Compostela, Santiago de Compostela, Spain | [2]Neuroimaging and Biotechnology Laboratory (NOBEL), Clinical Neurosciences Research Laboratory (LINC), Health Research Institute of Santiago de Compostela (IDIS), Santiago de Compostela, Spain | [3]Advanced (magnetic) Theranostic Nanostructures Lab, International Iberian Nanotechnology Laboratory, Braga, Portugal

Correspondence: Pelayo García-Acevedo (pelayo.garcia.acevedo@usc.es; pelayo.garcia.acevedo@sergas.es) | José Rivas (jose.rivas@usc.es)

Received: 12 August 2025 | **Revised:** 23 December 2025 | **Accepted:** 14 January 2026

Keywords: contrast agents | ligand exchange | magnetic contrast agents | magnetic resonance | ultra high field-MRI

ABSTRACT

Ultra-high-field magnetic resonance imaging (UHF-MRI, $B_0 > 7$ T) combined with contrast enhancement (CE-MRI) offers unmatched spatial resolution, but high-field effects limit the performance of negative contrast agents. Here, we report a ligand-driven strategy to modulate the T_2 relaxivity (r_2) of monodisperse 12 nm iron oxide-based contrast agents synthesized by thermal decomposition. Five surface chemistries–polyacrylic acid (PAA), poly(isobutylene-alt-maleic anhydride) (PMA), poly(maleic anhydride-alt-1-octadecene) (PMAO), citric acid (CA), and silica (SiO_2)— were investigated under physiological conditions and in vivo using relaxometry (1.4 T), clinical (3 T), and UHF (9.4 T) MRI, achieving up to a 333 mM^{-1} s^{-1} increase in r_2. CA-coated T_2 contrast agents exhibited record-high r_2 values (522 mM^{-1} s^{-1} at 3 T; 381 mM^{-1} s^{-1} at 9.4 T) in spherical iron oxide MNPs within the superparamagnetic size range ($d < 20$ nm). Correlations of r_2 with hydrodynamic size, ζ-potential, and coating thickness revealed that ligand chemistry–specifically hydrophilicity and anionic surface charge–dominates over physical shell dimensions in governing water accessibility and magnetic dephasing. This scalable ligand-exchange strategy enables precise T_2 tuning at UHF, with phantom results reliably predicting in vivo UHF-MRI performance in rat brain models, advancing the design of neuroimaging nanoprobes.

1 | Introduction

Magnetic resonance imaging (MRI)-based techniques have been widely used in disease diagnosis and monitoring due to their non-invasive nature, absence of ionizing radiation, and high spatial and temporal resolution [1–4]. However, alternative modalities such as computed tomography (CT) and positron emission tomography have driven continuous MRI development. Ultra-high-field-MRI (UHF-MRI, $B_0 > 7$ T) has recently emerged as an advanced imaging modality [5–7], characterized by improved spatial resolution and increased signal-to-noise ratio (SNR). Since FDA approval in 2017, UHF-MRI has gained clinical relevance [8–12]. Its combination with CE-MRI, enabled by contrast agents, further improves tissue visibility and signal modulation, enhancing diagnostic accuracy [13, 14]. Contrast agents modulate hydrogen proton relaxation times, essential for image contrast, and are classified into T_1 agents (bright signals) and T_2 agents (dark signals) [15]. Iron oxides magnetic nanoparticles (MNPs) stand out as versatile contrast agents, primarily functioning as negative contrast agents (T_2 enhancement), while recent advances–including exceedingly small magnetic iron oxide nanoparticles (ES-MIONs)–have enabled positive T_1 contrast

[16–22]. Beyond imaging, MNPs also offer multifunctional therapeutic applications such as magnetic hyperthermia [23–25], drug delivery [26–28], gene therapy, or as cell trackers [29].

The study and translation of T_1 and T_2 effects in UHF-MRI have become particularly relevant, as they aim to enhance tissue differentiation and enable higher spatial resolution for the precise detection of small lesions and complex structures [30–32]. However, this translation remains challenging for iron oxide-based contrast agents due to UHF-induced effects. Well-defined iron oxide MNPs exhibit high magnetic susceptibility, which can limit their utility as T_2 contrast agents due to magnetic saturation and motional averaging effects related to the high Larmor frequency [1, 33, 34]. Additionally, iron oxide MNPs have been investigated in core–shell architectures for T_1–T_2 dual contrast [35, 36]–a strategy developed to overcome the limitations of single-mode MRI [37–40]. However, the strong T_2 effect can dominate, reducing M_Z recovery and attenuating T_1 contrast agent relaxation [37], a phenomenon further amplified under UHF-MRI conditions [5, 6]. Therefore, precise modulation of T_2 performance in iron oxide MNPs is of particular interest at UHF. This is not only to improve their T_2 contrast efficiency in UHF-MRI, but also to enable "magnetic neutralization" in dual-mode designs.

Recent studies have shown promising results based on structural modification of T_2 contrast agents, particularly through atom-by-atom manipulation, as well as dopant effects [5, 41, 42]. However, the clinical translation of any material requires the search for simple, accessible, and cost-effective methods. Therefore, tuning the magnetic moment magnitude through precise control of the mesoscopic characteristics of iron oxide-based contrast agents offers a potentially more effective approach. In this context, ligand exchange has been extensively explored as a method to adjust the colloidal stability and prevent aggregation of iron oxide-based MNPs [43–47]. These surface modifications–along with changes in particle size, coating properties, and functional groups–could significantly influence MRI contrast performance. However, the relationship between these parameters and MRI efficiency remains complex and not fully understood. Recent work has highlighted the role of surface chemistry–particularly the molecular weight and composition of surface coatings–in tuning the relaxivity of T_2 contrast agents (3.6 and 10.9 nm iron oxide-based MNPs) [48]. These effects appear to be size-dependent (ranging from 4 to 33 nm iron oxide-based MNPs) [49] and may be linked to alterations in surface spin dynamics [50]. Addressing current limitations, emerging systems such as ligand-mediated magnetism-conversion probes and pH- or dual-stimuli-activatable assemblies have shown enhanced responsiveness under UHF-MRI, emphasizing the pivotal role of surface chemistry in modulating magnetic behavior and contrast efficiency at high fields [51–53]. Nevertheless, consistent trends in colloidal behavior following ligand exchange remain elusive, and most studies have yet to determine how these insights translate under UHF-MRI or in vivo conditions, both essential for the development of next-generation T_2 contrast agents.

In this study, five different compounds– polyacrylic acid (PAA), poly(isobutylene-alt-maleic anhydride) (PMA), poly(maleic anhydride-alt-1-octadecene) (PMAO), citric acid (CA), and silica (SiO_2)– were used to explore how ligand exchange influences T_2 contrast performance from physiological conditions to in vivo environments, evaluating their effects under both clinical and UHF-MRI fields (Figure 1). The T_2 contrast agents were spherical iron oxide MNPs with a narrow size distribution (d = 12.3 ± 1.6 nm), synthesized via thermal decomposition. Relaxometric measurements (B_0 = 1.4 T) and MRI imaging (B_0 = 3.0 T and B_0 = 9.4 T) revealed the crucial role of ligand exchange in modulating T_2-weighted image efficiency, producing steep changes in r_2 and achieving some of the highest reported relaxivities for spherical iron oxide MNPs (r_2 = 522 $mM^{-1}\,s^{-1}$, B_0 = 3 T). Under UHF-MRI conditions, r_2 generally declined due to enhanced T_2 decay, though values remained above 200 $mM^{-1}\,s^{-1}$ in most cases. Notably, CA-coated MNPs exhibited the highest r_2 at 9.4 T (r_2 = 381 $mM^{-1}\,s^{-1}$), followed by PMA-coated MNPs (r_2 = 322 $mM^{-1}\,s^{-1}$), indicating that these coatings effectively optimize CE-MRI under UHF conditions. Translation to preclinical animal models, specifically targeting the brain, confirmed that surface-chemistry-driven mesoscopic effects persist in vivo, with strong negative contrast in T_2-weighted images and signal attenuation patterns closely matching phantom data. These findings highlight the predictive value of phantom-based assessments and reaffirm ligand exchange as a robust chemical strategy to tune T_2 contrast in iron oxide-based agents across clinical and UHF-MRI settings.

2 | Results and Discussion

2.1 | Design and Characterization of Ligand-Functionalized Iron Oxide Nanoprobes

The ligand exchange procedure was performed on 12 nm iron oxide-based T_2 contrast agents synthesized via the thermal decomposition method, characterized by a well-defined spherical morphology, non-aggregated dispersion (Figure 2a), and a narrow size distribution (Figure S1a). The crystal structure of the precursor MNPs corresponds to a cubic spinel crystallographic structure, consistent with the coexistence of both magnetite and maghemite phases (Figure 2c). The crystalline size was determined to be D_{XRD} = 10.3 nm for IO@OA MNPs, aligning with values obtained from D_{TEM}, albeit approximately 20% lower, suggesting that each nanoparticle consists of single crystals. The presence of a band at ~550 cm^{-1} in the FT-IR spectra (Figure 2b), corresponding to tetrahedral Fe^{3+}—O^{2-} stretching vibrations, confirms the presence of Fe oxide MNPs. Additional bands at 2914, 3843, 1516, and 1403 cm^{-1}, attributed to (—CH_2) stretching, the OA hydrocarbon chain, and COO^- groups, indicate surface functionalization with OA. Surface modification with five different coatings (PAA, PMA, PMAO, CA, and SiO_2) enabled transfer to aqueous media without observable alterations in morphology (Figure 2d) and with a well-maintained size distribution (Figure S1b–f). However, variations in the arrangement of T_2-contrast agents were observed, with noticeable aggregation in the IO@PAA MNPs.

These ligands differ in molecular weight, backbone structure, and functional groups, resulting in variations in coating thickness, hydration, and hydrophobicity. CA is a low-molecular-weight molecule (192 g mol^{-1}) bearing three carboxylic acid groups and one hydroxyl group, enabling multidentate coordination and the formation of a thin, highly hydrated interfacial layer. In

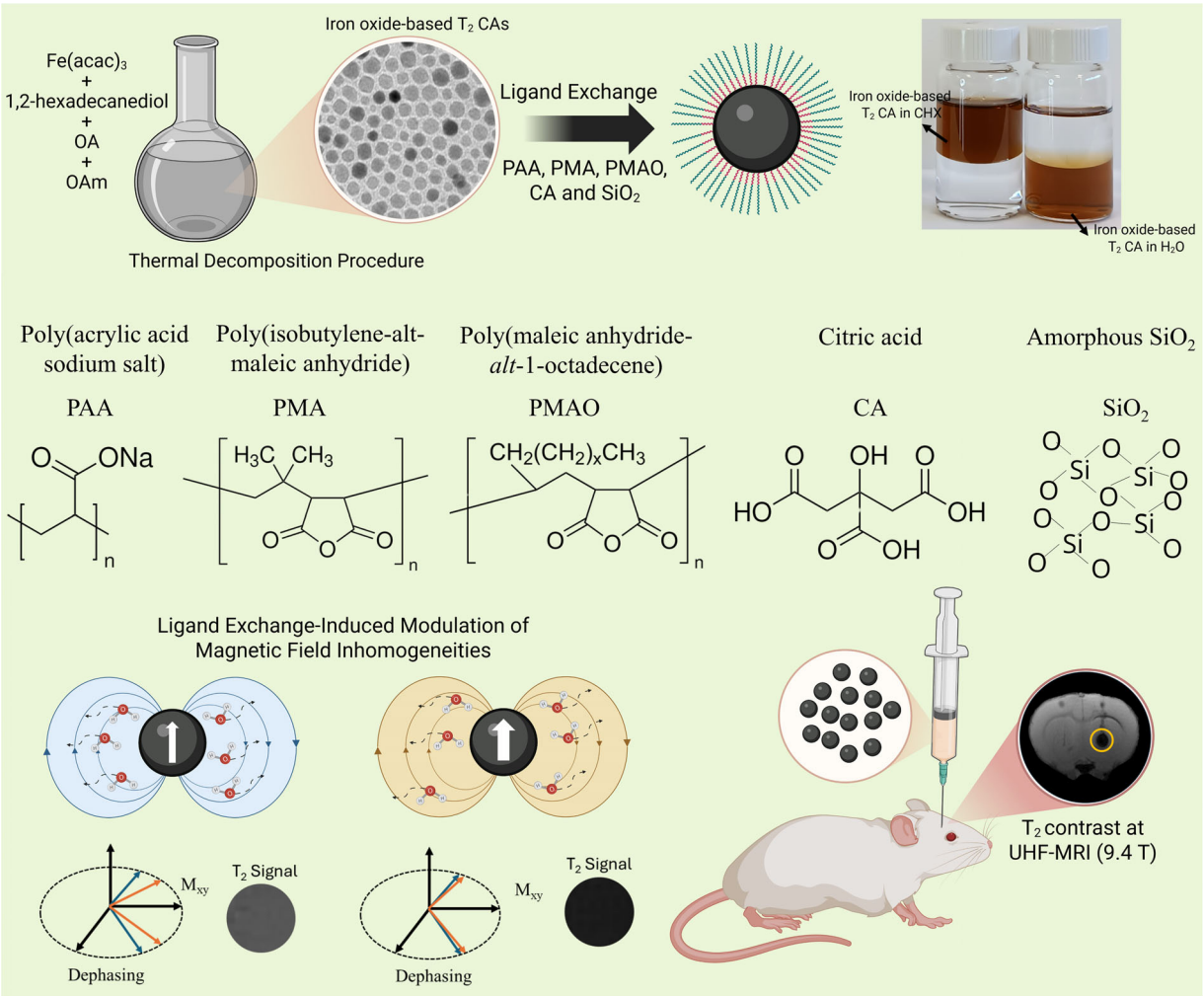

FIGURE 1 | Schematic illustration of the ligand exchange process on iron oxide MNPs using different surface coatings– PAA, PMA, PMAO, CA, and SiO_2–with their corresponding chemical structures shown to highlight functional groups and interactions with the nanoparticle surface. These coatings were employed to modulate the efficiency of iron oxide-based T_2 contrast agents under clinical and UHF conditions (B_0 = 9.4 T), and to evaluate their response to physiological conditions in in vivo preclinical models.

contrast, polymeric ligands such as PAA (5100 g mol^{-1}), PMA (~6000 g mol^{-1}), and PMAO (30 000–50 000 g mol^{-1}) possess extended carbon backbones with carboxylic or cyclic anhydride groups, forming thicker coatings and introducing hydrophobic segments that may reduce local hydration. The SiO_2 shell (~10 nm) constitutes an inorganic diffusion barrier, limiting water accessibility at the interface.

These structural differences are further corroborated by FT-IR spectroscopy, which confirms both the preservation of the iron oxide core and the successful surface functionalization (Figure S2). In all samples, the characteristic Fe—O stretching band in the 400–600 cm^{-1} region evidences the presence of the iron oxide core after coating. Coordination of the organic ligands is indicated by asymmetric and symmetric carboxylate stretching bands ($\nu_{as}(COO^-) \approx$ 1550–1625 cm^{-1} and $\nu_{sym}(COO^-) \approx$ 1400–1450 cm^{-1}), together with C—O vibrations at ~1000–1050 cm^{-1} associated with interfacial C—O—Fe bonding. IO@PAA MNPs exhibit a pronounced $\nu_{as}(COO^-)$ band at around 1624 cm^{-1}, while IO@PMA and IO@PMAO MNPs show similar features consistent with partial hydrolysis of maleic anhydride units. In IO@PMAO MNPs, strong C–H stretching bands at 2850–2950 cm^{-1} confirm the presence of long aliphatic chains, whereas a broad O—H band around 3400 cm^{-1} arises from surface hydroxyls and adsorbed water. The SiO_2 coating is identified by the dominant Si—O—Si stretching band at 1000–1100 cm^{-1}, consistent with a dense inorganic shell [54–57]. The aliphatic C–H stretching bands of oleic acid (≈2850–2920 cm^{-1}), prominent in the native OA-coated MNPs, are noticeably attenuated or masked after surface modification, reflecting partial ligand exchange or overcoating by amphiphilic polymers such as PMA and PMAO.

The influence of ligand exchange on the magnetic properties of iron oxide-based T_2 contrast agents was evaluated by measuring blocking temperature (T_B), saturation magnetization (M_S), remanence (M_R), and coercivity (H_C). These parameters were obtained from the hysteresis loop measurements (Figure 2e; Table S1). IO@OA MNPs exhibited $M_S > 80$ emu g^{-1}, close to bulk magnetite (92 emu g^{-1}), indicating high crystallinity. $M_R \approx 0$ and $H_C \approx 0$ confirmed superparamagnetic behavior at 300 K, while higher M_S and nonzero M_R and H_C indicated ferrimagnetism at 5 K. Post-ligand exchange, the hysteresis loops (Figure S3), did not reveal

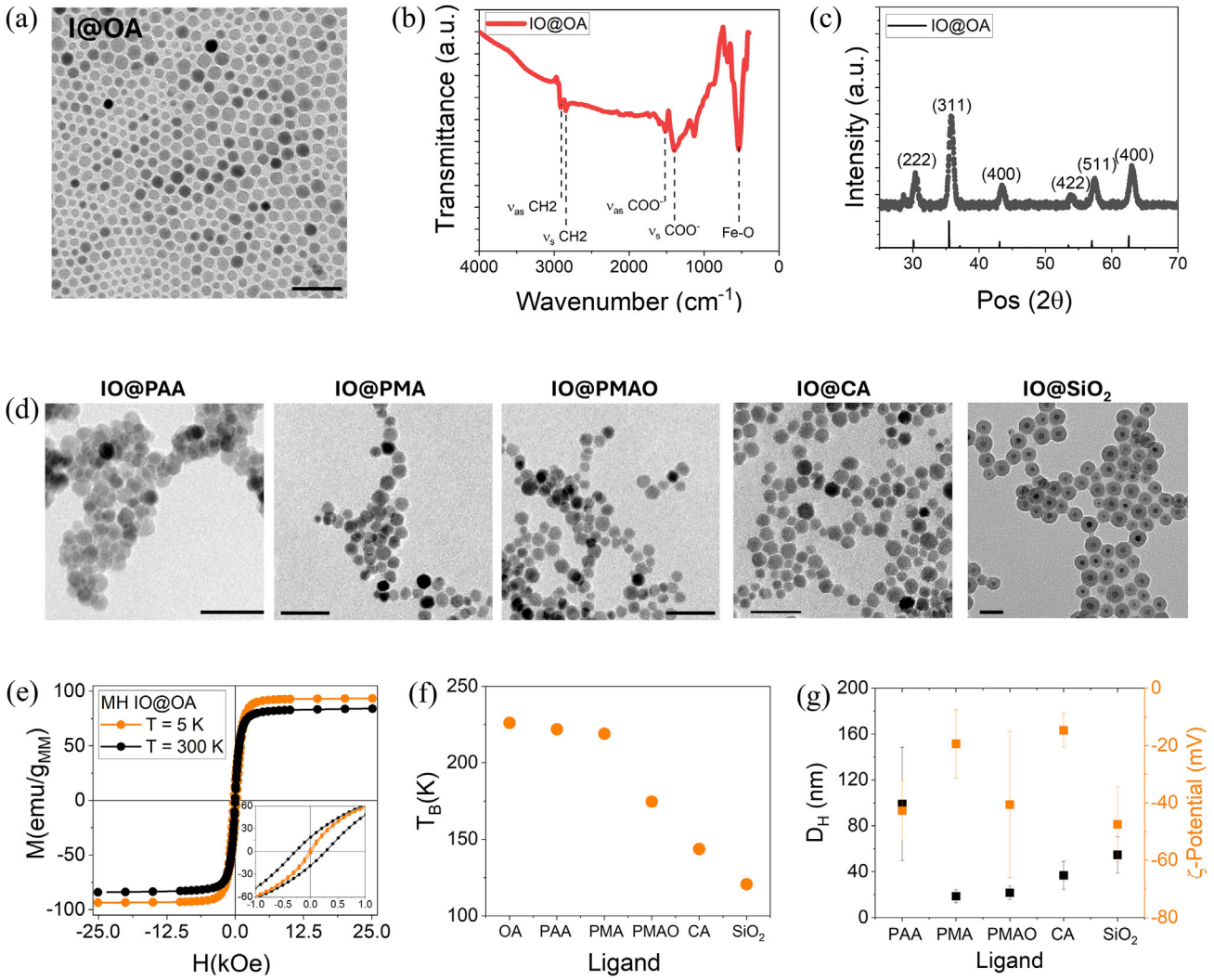

FIGURE 2 | (a) Representative TEM micrographs of the precursor IO@OA MNPs synthesized by thermal decomposition. (b) FTIR spectra and (c) X-ray diffraction patterns of IO@OA MNPs. The solid black line represents the magnetite reference pattern. (d) Representative TEM micrographs of iron oxide-based contrast agents after transferring to aqueous medium by ligand exchange. (e) Hysteresis loops developed at $T = 300$ K and $T = 5$ K of the IO@OA MNPs for applied magnetic fields between ±25 kOe. The insets represent a magnification of the hysteresis loops. (f) T_B obtained from the ZFC-FC curves of batches iron oxide-based contrast agents as a function of ligand. (g) Hydrodynamic size (black dots) and ζ-potential (orange dots) of iron oxide-based contrast agents as a function of the ligand used. Only for panel (g), data are shown as mean ± SD ($n = 3$); all other panels show representative images or individual measurements.

significant changes in M_S compared to the precursor MNPs, maintaining values close to 80 emu g^{-1} (at $T = 300$ K) and close to 93 emu g^{-1} (at $T = 5$ K). Additionally, M_R and H_C approached zero at $T = 300$ K, rising to significantly higher values at $T = 5$ K. ZFC-FC curves (Figure S4a) showed $T_B = 226$ K in precursor IO@OA T_2-contrast agents, confirming superparamagnetism at room temperature, essential for bioapplications. T_B variation with different ligands (Figure 2f) indicated minimal effects from PAA and PMA, whereas thick SiO_2 coatings (~10 nm) reduced T_B by >50%, decreasing dipolar interactions.

The dispersity and stability of the T_2 iron oxide-based contrast agents were evaluated using DLS measurements to determine the hydrodynamic size (D_H) and ζ-potential (Figure 2g; Figure S5; Table 1). PMA, PMAO, and SiO_2 ligands provided better colloidal stability, with low *PDI* (<0.1) and D_H values around 20 nm for PMA and PMAO, and 50 nm for SiO_2. In contrast, PAA-functionalized MNPs exhibited higher D_H and *PDI* values, correlating with aggregates observed in TEM images. The ζ-potential values, generally above −30 mV, confirmed stable dispersions due to electrostatic repulsion, with all MNPs exhibiting negative surface charges. Negatively charged iron oxide MNPs are particularly suitable for biomedical applications, as they combine prolonged circulation, reduced uptake by the reticuloendothelial system, and minimized nonspecific interactions with proteins and cells, while maintaining low cytotoxicity. In contrast, positively charged MNPs tend to interact strongly with cell membranes, accumulate rapidly in organs, and are eliminated quickly, limiting their practical use [58–65]. These properties provide a clear rationale for employing negatively charged iron oxide MNPs in biomedical imaging.

TABLE 1 | Nanoparticle size obtained by TEM micrographs (D_{TEM}) and its corresponding PDI_{TEM}; hydrodynamic size (D_H) and its corresponding PDI_{DLS}, obtained by DLS; and ζ-potential values of MNPs, and the estimation of the shell thickness δ_{shell}. *For the IO@SiO_2 sample, due to its inorganic nature and the possibility of direct visualization by TEM, the shell thickness was directly measured from TEM images.

Sample	D_{TEM} (nm)	δ_{th} (nm)	PDI_{TEM}	D_H (nm)	PDI_{DLS}	ζ-Potencial (mV)
IO@OA	12.3 ± 1.6	2.2	0.02	—	—	—
IO@PAA	12.6 ± 1.3	1.7	0.01	99.1 ± 49.2	0.25	−42.7 ± 10.6
IO@PMA	13 ± 1.7	2.5	0.02	18.5 ± 5.8	0.09	−19.4 ± 11.9
IO@PMAO	13.5 ± 1.6	7.6	0.01	21.6 ± 5.9	0.07	−40.6 ± 25.5
IO@CA	12.9 ± 1.9	1.6	0.02	36.8 ± 12.3	0.11	−14.7 ± 5.9
IO@SiO_2	33.2 ± 3.9 (*)	10.3(*)	0.01	54.5 ± 15.7	0.08	−47.5 ± 13

TGA analysis (Figure S6; Table S2) provided insights into the surface structure of the iron oxide-based T_2 contrast agents before (OA coating) and after (PAA, PMA, PMAO, CA, SiO_2) transfer to aqueous media. Two distinct mass loss phases were observed: 60°C–200°C, corresponding to adsorbed solvents, and 200°C–400°C, associated with organic ligand decomposition. In this early stage of the temperature ramp, precursor IO@OA MNPs exhibited weight losses of 12%, while functionalized T_2 contrast agents with PAA and CA showed lower losses, confirming OA removal. MNPs with PMA and PMAO showed higher losses, indicating successful ligand anchoring, and SiO_2 showed the lowest weight loss (8%). At 800°C, organic matter was fully decomposed, and the mass remaining was attributed to Fe oxide. The functionalized MNPs with PAA and CA showed lower losses (<25%), while those with PMA and PMAO showed higher losses (>30%). The inorganic SiO_2-coated contrast agents showed losses of around 10%. By combining TEM data, MNP density (ρ_{Fe3O4} = 5.17 g cm^{-3}), and TGA concentration, the ligand shell thickness (δ_{th}) was calculated, considering the organic mass loss (Table 1). SiO_2 thickness was directly measured from TEM. The thinnest coatings were found in IO@CA (δ_{th} = 1.7 nm), while the thickest were in IO@PMAO (δ_{th} = 7.6 nm). In general, PAA and CA functionalized MNPs had thinner coatings, while PMA and PMAO showed thicker coatings, confirming their amphiphilic nature and resistance to OA removal.

2.2 | MRI Characterization of Ligand-Functionalized Iron Oxide Nanoprobes

The transverse relaxation properties of iron oxide-based T_2 contrast agents were evaluated through relaxometry techniques at B_0 = 1.4 T (Figure 3a) and MR imaging at clinically relevant (B_0 = 3 T, Figure 3b) and UHF conditions (B_0 = 9.4 T, Figure 3c). The linear dependence of $1/T_2$ on iron concentration enabled the determination of transverse relaxivity (r_2), revealing a significant dependence on both the applied field and surface functionalization. T_2 parametric maps acquired at B_0 = 3 T and B_0 = 9.4 T (Figure 3d) illustrate the spatial distribution of relaxation values as a function of Fe concentration. The extracted r_2 (Figure 3e; Table 2) indicates that at B_0 = 1.4 T, PMA-coated MNPs exhibit the highest relaxivity (r_2 = 277 mM^{-1} s^{-1}) followed by PAA and CA-functionalized MNPs.

At B_0 = 3 T, a marked increase in r_2 was observed for CA-functionalized MNPs (r_2 = 522 mM^{-1} s^{-1}), which surpasses all other ligands, highlighting the enhanced efficiency of these MNPs under clinically relevant field conditions. The superior transverse relaxivity of CA-functionalized MNPs at 3 T likely arises from the multidentate coordination and minimal steric hindrance of the thin citric acid layer, which promotes efficient interaction of water protons with the magnetic core, consistent with the chemical and structural features discussed previously. IO@PMA MNPs also exhibit an increase in r_2 (r_2 = 378 mM^{-1} s^{-1}), while PMAO and PAA remain relatively unchanged ($r_2 \approx$ 200 mM^{-1} s^{-1}). Interestingly, SiO_2-coated MNPs exhibited a substantial increase in r_2 (r_2 = 289 mM^{-1} s^{-1}), despite their inorganic and relatively impermeable nature. This suggests that the silica shell may influence relaxivity not only by modulating water accessibility but also by altering the local magnetic environment. Although moderate increases in r_2 are expected up to 3 T due to enhanced dephasing effects, the relatively high r_2 value observed for SiO_2 coatings–compared to organic ligands–may also reflect changes in the effective magnetization of the nanoparticle core, potentially due to altered surface interactions or aggregation behavior induced by the rigid shell.

In the UHF regime (B_0 = 9.4 T), a significant decline in r_2 was observed for most formulations. CA-functionalized MNPs retain the highest relaxivity (r_2 = 381 mM^{-1} s^{-1}), albeit lower than at B_0 = 3 T, reinforcing their robustness across different fields. PAA- and PMAO-coated MNPs did not exhibit the r_2 reduction under UHF-MRI conditions that has been observed in the other functionalized T_2 contrast agents, a behavior generally attributed to enhanced susceptibility-related effects and, more recently, to the contribution of interparticle dipolar interactions [66]. For IO@PAA, this behavior could be related to ligand-induced aggregation, as evidenced by increased D_H from DLS measurements and higher T_B in magnetic characterization. This pre-existing aggregation may mask additional field-induced aggregation effects, helping maintain r_2 across different magnetic fields. For IO@PMAO, the relatively bulky nature of the PMAO ligand, with partially hydrophobic segments, may help preserve the colloidal structure across increasing magnetic field strengths and limit variations in water accessibility at the nanoparticle interface under UHF conditions.

The obtained r_2 = 522 mM^{-1} s^{-1} (B_0 = 3 T) for CA-functionalized MNPs ranks among the highest reported for conventional, spherical and superparamagnetic iron oxide MNPs (<20 nm). For

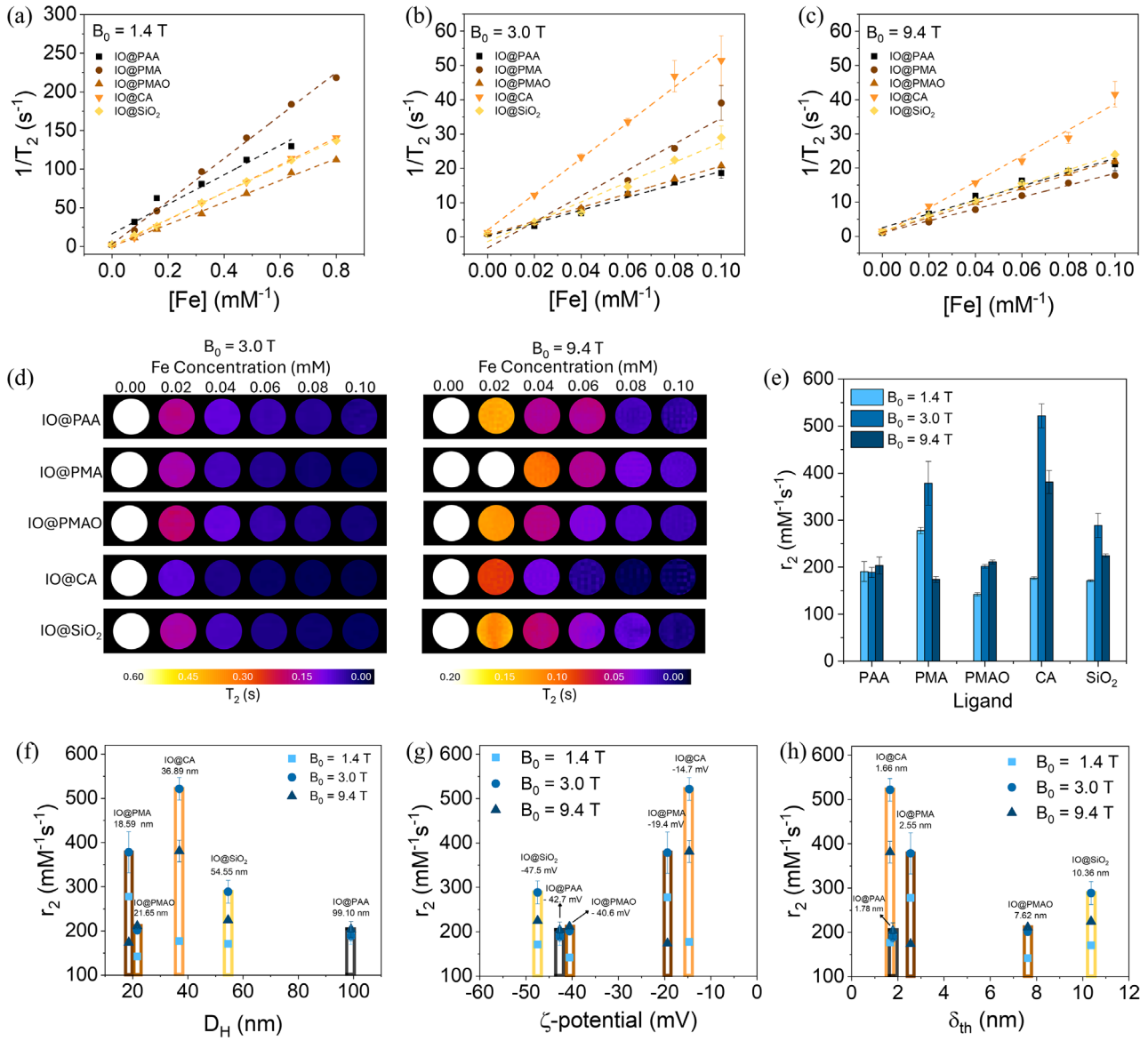

FIGURE 3 | Inverse of transverse relaxation time ($1/T_2$) obtained by (a) relaxometry measurements at $B_0 = 1.4$ T and by the MR images at (b) $B_0 = 3$ and (c) $B_0 = 9.4$ T as a function of the Fe concentration for the different ligand-functionalized MNPs. (d) T_2 maps (color-mapped image) of the iron oxide-based contrast agents at different concentrations from 0 mM (H_2O) to 0.1 mM at $B_0 = 3$ T (left) and $B_0 = 9.4$ T (right). Dependence of r_2 with (f) D_H, (g) ζ-Potential, and (h) δ_{th} obtained at $B_0 = 1.4$, 3, and 9.4 T of iron oxide-based T_2 contrast agents. Data are shown as mean ± SD ($n = 3$).

reference, the highest r_2 values reported to the best of our knowledge for MNPs with similar characteristics typically range from 300 to 425 $mM^{-1}\ s^{-1}$. Specifically, for MNPs smaller than 10 nm, r_2 values of 355 $mM^{-1}\ s^{-1}$ (8 nm, $B_0 = 3$ T) [67] and up to 425 $mM^{-1}\ s^{-1}$ (9 nm, $B_0 = 1.5$ T) [68] have been observed. In the 10–15 nm range, r_2 values of 385 and 360 $mM^{-1}\ s^{-1}$ (both 14 nm, $B_0 = 0.47$ T) [69, 70] have been reported, while MNPs larger than 15 nm show r_2 values between 276 and 385 $mM^{-1}\ s^{-1}$, depending on particle size, coating, and applied field [49, 71–74].

Some non-conventional nanosystems reach even higher r_2 values, exceeding those reported in this work. These include cation-doped spinel ferrite nanoparticles such as $Zn_{0.3}\ Mn_{0.7}\ Fe_2\ O_4$ (15 nm, $r_2 = 860\ mM^{-1}\ s^{-1}$) and $Zn_{0.4}\ Fe_{0.6}\ Fe_2\ O_4$ (15 nm, $r_2 = 687\ mM^{-1}\ s^{-1}$) [73], anisotropic morphologies such as nanocubes (22 nm, $r_2 = 761\ mM^{-1}\ s^{-1}$) or octapods (30 m, $r_2 = 989\ mM^{-1}\ s^{-1}$) [75, 76], nanoclusters (181 nm,

TABLE 2 | Transversal relaxivities (r_2) obtained by the MR images and relaxometry measurements of the iron oxide-based T_2 contrast agents. $\Delta\omega\tau_D$ estimated from the effective size of the MNPs, considered as the hydrodynamic diameter (D_H).

Sample	1.4 T r_2 ($mM^{-1}\ s^{-1}$)	3 T r_2 ($mM^{-1}\ s^{-1}$)	9.4 T r_2 ($mM^{-1}\ s^{-1}$)	$\Delta\omega\tau_D$
IO@PAA	191 ± 21	189 ± 11	203 ± 18	39.1
IO@PMA	278 ± 6	378 ± 46	174 ± 6	1.3
IO@PMAO	142 ± 4	202 ± 4	211 ± 4	1.8
IO@CA	177 ± 3	522 ± 25	381 ± 24	5.4
$IO@SiO_2$	171 ± 2	289 ± 26	225 ± 4	11.8

r_2 = 604 mM^{-1} s^{-1}) [77] and spherical MNPs outside the superparamagnetic regime (33 nm, r_2 = 510 mM^{-1} s^{-1}) [49]. However, they do not always guarantee an optimal balance between efficiency and safety, as the presence of cations in spinel ferrites can increase cytotoxicity [78], non-spherical morphologies may affect cellular uptake and toxicological profile [79, 80], and some nanocluster systems do not meet the size requirements to cross physiological barriers such as the blood–brain barrier (<100 nm) [81] for neurological applications.

2.3 | Correlation Between Physicochemical Properties and MRI Performance of Ligand-Functionalized Iron Oxide Nanoprobes

To elucidate the relationship between the physicochemical properties of iron oxide-based T_2 contrast agents and their efficiency in MRI, r_2 was analyzed as a function of D_H (Figure 3f), ζ-potential (Figure 3g), and δ_{th} (Figure 3h). The dependence of r_2 on D_H does not follow a monotonic trend, suggesting that nanoparticle size alone does not dictate relaxation efficiency. A correlation between r_2 and ζ-potential was observed, where MNPs exhibiting more negative surface charges showed higher r_2 values. This effect may be attributed to enhanced water proton accessibility and mobility near the nanoparticle surface, which facilitates spin–spin relaxation. Strongly negative ζ-potentials promote electrostatic attraction of positively charged water protons, leading to increased local water density at the particle-solvent interface. This, in turn, could enhance the dephasing effect caused by the local magnetic field inhomogeneities generated by the nanoparticle core.

Despite the expected inverse relationship between coating thickness and r_2, the observed trend was not straightforward. While thicker coatings are generally believed to restrict water access and reduce r_2, this pattern does not hold consistently across different ligands. For instance, IO@PAA, with δ_{th} = 1.7 nm, exhibits a lower r_2 value compared to IO@PMAO and IO@SiO$_2$ despite having a greater thickness. Interestingly, IO@CA, with a thinner coating of only 1.6 nm, shows the highest r_2, indicating that the chemical nature of the ligand plays a more significant role in determining the water–ligand interactions and contrast efficiency.

The effect of the magnetic field on proton relaxation is modeled through Larmor frequency dispersion ($\Delta\omega$). MRI contrast efficiency depends on the time protons remain in these magnetically influenced regions (τ_D). If the Redfield condition ($\Delta\omega\tau_D \ll 1$) is met, r_2 follows the outer sphere model or motional averaging regime (MAR), expressed as [1, 49, 82]:

$$r_2 = \frac{4v_{mat}(\gamma_H \mu_0 M_V d)^2}{450 D_{bulk}} \quad (1)$$

where γ_H is the ^{1}H gyromagnetic ratio, μ_0 is the vacuum permeability, D is the water diffusion coefficient, v_{mat} is the molar volume of magnetic ions, d is the nanocrystal diameter, and M_v is the volumetric saturation magnetization. If $\Delta\omega\tau_D > 1$, the system enters the static dephasing regime (SDR), where r_2 stabilizes. For $\Delta\omega\tau_D > 20$, in the echo-limited regime (ELR), r_2 decreases with increasing size, which should be avoided in contrast agent design. To maximize r_2, MNPs should meet the SDR constraint with $5 \leq \Delta\omega\tau_D \leq 20$, corresponding to optimal sizes between 36–72 nm [49], while avoiding non-superparamagnetic particles with significant coercivity. Additionally, MNP clustering can alter r_2, making the choice of nanoparticle coating crucial for MRI efficiency. To investigate the influence of ligands on r_2 modulation, the impact on $\Delta\omega\tau_D$ was analyzed. The resulting r_2 values depend on the dynamic regime of the MNPs, such as MAR, ELR, or SDR. $\Delta\omega\tau_D$ was obtained, assuming $\gamma_H = 2.68 \times 10^8$ rad T^{-1} s^{-1}, $\mu_0 = 4\pi \times 10^{-7}$ T m A^{-1}, $D_{bulk} = 3.1 \times 10^{-9}$ m^2 s^{-1} at 37°C, approximating M_v to $M_v \approx 4.26 \times 10^5$ A m^{-1} with d = 12.07 nm, obtained from the magnetic cores IO@OA, respectively. Specifically, the calculated values were $\Delta\omega\tau_D \approx 0.5$. According to this, r_2 should be described by the MAR regime, with d and M_V dominating the modulation of r_2.

To understand the role of the employed ligand, $\Delta\omega\tau_D$ was obtained considering the effective particle size of each MNP, approximated to D_H (Table 2). IO@PAA exhibited the highest $\Delta\omega\tau_D$ ($\Delta\omega\tau_D$ = 39.1), placing it in the ELR regime, with a moderate r_2 (r_2 = 203 mM^{-1} s^{-1}, B_0 = 9.4 T). Conversely, IO@PMA and IO@PMAO displayed lower $\Delta\omega\tau_D$ ($\Delta\omega\tau_D$ = 1.3 and $\Delta\omega\tau_D$ = 1.8, respectively), situating them near the MAR-SDR boundary, which correlates with their reduced r_2 . IO@SiO$_2$, ($\Delta\omega\tau_D$ = 11.8), exhibited a lower r_2 , suggesting that the SiO$_2$ shell limits water accessibility, shifting its regime toward SDR. Interestingly, IO@CA displayed an elevated r_2 (r_2 = 381 mM^{-1} s^{-1}, B_0 = 9.4 T) despite a moderate $\Delta\omega\tau_D$ ($\Delta\omega\tau_D$ = 5.4), indicating contributions from ligand-induced effects, such as colloidal stability or local magnetic interactions.

In summary, CA-functionalized MNPs exhibited the highest r_2 across clinically relevant and UHF fields, reflecting the efficiency of thin citric acid layers in enhancing water–ligand interactions and proton relaxation. SiO$_2$-coated MNPs, despite their relatively thick inorganic shell, also showed enhanced r_2, indicating that silica surface chemistry, likely through silanol groups, promotes water accessibility and proton mobility at the nanoparticle interface. Organic ligand coatings such as IO@PAA and IO@PMAO, however, possess thinner shells but lower r_2, highlighting that ligand hydrophilicity and chemical composition, rather than coating thickness alone, govern relaxation efficiency. Additionally, the correlation between a more negative ζ-potential and elevated r_2 underscores the contribution of electrostatic effects. Together, these results demonstrate that ligand surface chemistry–particularly hydrophilicity and surface charge of anionic MNPs–dominates the modulation of transverse relaxivity.

2.4 | In Vivo MRI Performance of Ligand-Functionalized Iron Oxide Nanoprobes

The translation of the observed effects in physiological environments must be demonstrated in preclinical models. To achieve this, the efficiency of iron oxide-based T_2 contrast agents was explored in vivo through a proof-of-concept study in animal models, specifically targeting the brain. The different iron oxide-based T_2 contrast agents were injected into the right hemisphere of the brain (10 µL, 0.5 mM Fe, n = 3), with a PBS injection used as a control in the left hemisphere. The effect of the

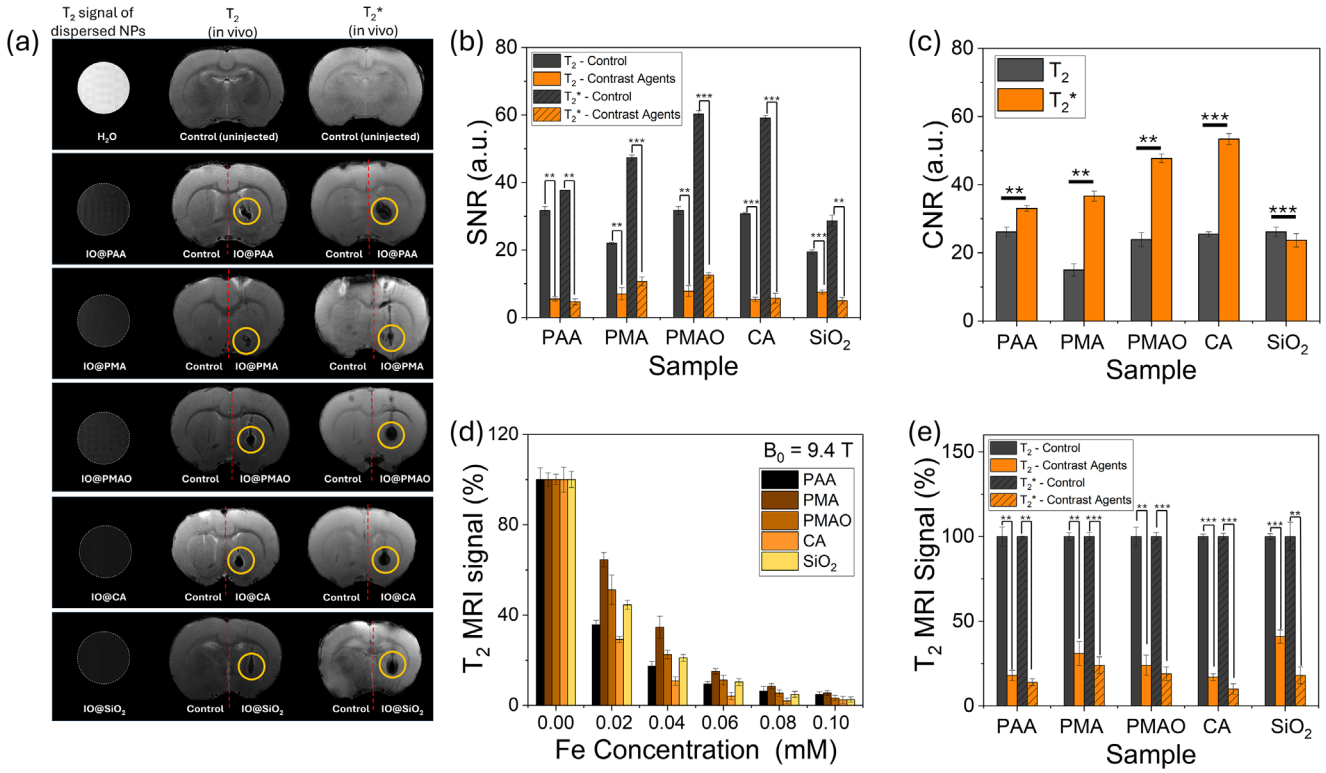

FIGURE 4 | (a) Representative T_2-weighted (left) and T_2*-weighted (right) MR images of rat brains (coronal plane) after injection of iron oxide-based T_2-contrast agents into the right hemisphere and PBS into the left hemisphere. Yellow circles highlight regions of hypointensity due to iron oxide nanoparticle accumulation. Corresponding phantom images of each iron oxide nanoformulation dispersed in H_2O are shown on the far left. (b) SNR and (c) CNR derived from T_2- and T_2*-weighted MRI after intracerebral injection of iron oxide-based T_2 contrast agents (0.5 mM Fe) (d) T_2-weighted MR signal intensity of phantom samples containing iron oxide MNPs coated with different ligands: PAA, PMA, PMAO, CA, and SiO_2 obtained from T_2-weighted MR images (Figure S6). (e) Normalized in vivo T_2- and T_2*-weighted MRI signal intensity obtained from rat brains after intracerebral injection of iron oxide-based T_2- contrast agents (0.5 mM Fe). Signal intensities in both (d,e) were normalized to the H_2O (phantom) and PBS (in vivo) controls, set to 100%. Data are shown as mean ± SD ($n = 3$). Statistical significance is indicated by asterisks (*$p < 0.05$, **$p < 0.01$, ***$p < 0.001$; ns, not significant).

TABLE 3 | Normalized T_2 and T_2* signal intensities (% ± SD) and contrast-to-noise ratio (CNR, mean ± SD) for iron oxide-based T_2 contrast agents in phantom (0.04 mM Fe) and in vivo (T_2 and T_2* after intracranial injection, 0.5 mM Fe, 10 μL).

Sample	Normalized T_2 Signal-Phantom (%)	T_2 CNR-in vivo (a.u.)	T_2* CNR-in vivo (a.u.)	Normalized T_2 Signal-in vivo (%)	Normalized T_2* Signal-in vivo (%)
IO@PAA	17 ± 2	26 ± 1	33 ± 1	18 ± 3	14 ± 2
IO@PMA	35 ± 5	15 ± 2	37 ± 1	31 ± 7	24 ± 5
IO@PMAO	22 ± 2	24 ± 2	48 ± 1	24 ± 6	19 ± 4
IO@CA	10 ± 2	25 ± 1	53 ± 2	17 ± 2	10 ± 3
IO@SiO_2	21 ± 2	26 ± 1	24 ± 2	41 ± 4	18 ± 5

T_2 contrast agents was demonstrated by the observation of a strong negative contrast in the T_2-weighted and T_2*-weighted in vivo MR images of rat brains after intracranial injections (Figure 4a).

Following the qualitative observation of signal hypointensity, a quantitative analysis was performed by evaluating the SNR and contrast-to-noise ratio (CNR) in the injected brain regions (Table 3; Figure 4b,c; details of SNR and CNR calculation are provided in the Materials and Methods section). In T_2-weighted images, SNR was markedly reduced after injection of contrast agents, with PMAO- and CA-functionalized MNPs producing the most pronounced signal attenuation (from ~31 a.u. to ~7 a.u.). In T_2*-weighted images, the stronger effect of PMAO- and CA-functionalized MNPs was even more evident (from ~60 to ~13 a.u.). Consistent with these trends, the CNR analysis, which normalizes the signal variations relative to the contralateral control, revealed enhanced contrast generation for PMAO- and CA-functionalized MNPs, particularly in T_2*-weighted images, reaching values of 48 and 53 a.u., respectively, in agreement with trends observed under physiological conditions in phantom experiments at UHF-MRI.

To further deepen the analysis and gain a more direct measure of the signal reduction induced by the contrast agents, the variation in the normalized signal relative to the control region of interest (ROI) was calculated (Table 3), revealing ligand-dependent signal variations (Figure 4e). These in vivo observations were in good agreement with the phantom results obtained for the same nanoparticle formulations dispersed in aqueous media (Figure 4d; Figure S7). Under physiological conditions, all iron oxide-based contrast agents exhibited a concentration-dependent reduction in T_2 signal intensity, with clear differences observed across surface ligands. This trend was comparable to the reduction in T_2 signal observed in vivo. The corresponding in vivo values were 18% for IO@PAA, 31% for IO@PMA, 24% for IO@PMAO, 17% for IO@CA, and 41% for IO@SiO_2. Taken together, the phantom calibration curve provides a quantitative framework to estimate the effective local concentration of iron oxide-based contrast agents in brain tissue from the observed in vivo signal attenuation, suggesting an apparent concentration of approximately 0.04 mM despite an injected dose of 0.5 mM, while acknowledging limitations due to tissue heterogeneity and diffusion. At 0.04 mM in the phantom experiments, the normalized MR signal decreased to 17% for IO@PAA, 35% for IO@PMA, 22% for IO@PMAO, 10% for IO@CA, and 21% for IO@SiO_2. This correspondence at differing nominal concentrations suggests that the effective local concentration of iron oxide-based contrast agents in brain tissue is substantially lower than the administered dose, likely due to limited diffusion, tissue retention, or partial leakage during injection.

The modulation induced by ligand exchange remained the primary determinant of T_2 contrast efficiency in vivo. Consistent with its higher susceptibility sensitivity, T_2*-weighted imaging at UHF generated stronger contrast than conventional T_2-weighted scans. Notably, the ligand-dependent performance observed in phantom studies translated seamlessly to the brain, with CA-functionalized MNPs achieving the highest efficiency under complex tissue conditions. These findings underscore the predictive value of phantom assays, particularly at sub-maximal concentrations, and highlight surface chemistry as a crucial factor for optimizing T_2 contrast agents in translational UHF-MRI applications.

2.5 | Biosafety and Biodistribution Assessment of Ligand-Functionalized Iron Oxide Nanoprobes

To evaluate the biosafety of the contrast agents and the potential effects of ligand variation, serum levels of glutamate oxaloacetate transaminase (GOT), urea, and creatinine were measured in Sprague–Dawley rats as indicators of hepatic and renal injury. Measurements were taken at baseline and after intravenous administration of the contrast agents (1 mL, 2.5 mM Fe), revealing no significant differences in GOT levels among the different ligands (Figure 5a). A slight transient increase was detected during the early post-injection period, particularly at 4 h, followed by a return to baseline values at 24 h. Importantly, GOT values remained below the established toxicity reference level for the experimental set (92 U L^{-1}) throughout the study, suggesting the absence of significant hepatotoxicity for all contrast agents. Renal function was assessed by measuring serum urea, which exhibited a trend similar to that observed for GOT, with a slight transient increase exceeding the reference level (29 mg dL^{-1}) in some animals during the first hours post-injection, but returning to near-baseline values by 24 h (Figure 5b). This pattern indicates a temporary physiological response rather than sustained renal damage, as further evidenced by creatinine levels, remaining below the detection limit of the assay (<0.5 mg dL^{-1}).

On the other hand, CA-functionalized T_2 contrast agents were selected due to their superior contrast performance to evaluate their in vivo biodistribution by MRI. Biodistribution was assessed by comparing pre-injection and post-injection T_2-weighted MR images acquired 30 min after intravenous administration of IO@CA MNPs (2.5 mM Fe, 1 mL), evaluating the signal changes in various organs, including the brain, liver, kidneys, and lungs (Figure 5d). Changes in SNR, reflected as image darkening, were used as an indicator of nanoparticle accumulation (Figure 5c). A pronounced decrease in the T_2 signal was primarily observed in the liver and, to a lesser extent, in the kidneys, suggesting preferential accumulation of the MNPs in major metabolic and filtration organs.

Although the present study does not provide an exhaustive evaluation of the metabolic fate of the engineered contrast agents, their clearance mechanisms have been extensively described. Iron oxide-based MNPs are eliminated primarily via renal excretion when their hydrodynamic size permits, or through the mononuclear phagocyte system, where macrophages internalize and enzymatically degrade them within lysosomes. The released iron is subsequently incorporated into physiological pathways, including ferritin storage and transferrin-mediated transport [83–85]. In the central nervous system, MNP clearance occurs mainly through the perivascular glymphatic system and meningeal/cervical lymphatic network, allowing drainage from brain parenchyma to deep cervical lymph nodes. Microglial cells can also internalize MNPs, degrading them lysosomally and gradually releasing iron into intracellular metabolism, paralleling peripheral macrophage pathways and limiting long-term accumulation and neurotoxic risk [86–88]. Future studies addressing the impact of targeting ligands on cerebral nanoparticle metabolism, clearance pathways, and microglial processing would provide valuable mechanistic insight.

3 | Conclusion

In summary, this work demonstrates that chemical modification of iron oxide nanoparticles through ligand exchange is an effective strategy to modulate their T_2 contrast efficiency, particularly under UHF-MRI conditions, where T_2 signal decay becomes increasingly pronounced and challenging to manage. By varying only the surface ligand–using PAA, CA, PMA, PMAO, or SiO_2–significant differences in r_2 relaxivity were achieved, with values ranging from 188 to 521 mM^{-1} s^{-1} at 3 T (clinical field), and from 173 to 380 mM^{-1} s^{-1} at 9.4 T (UHF-MRI). These findings highlight the mesoscopic influence of surface chemistry on magnetic performance, underscoring the need for precise control over relaxation behavior in the design of contrast agents for UHF imaging. To assess the biological relevance of these physicochemical optimizations, the different nanoparticle formulations were evaluated in vivo via injection in rat brains under UHF-MRI.

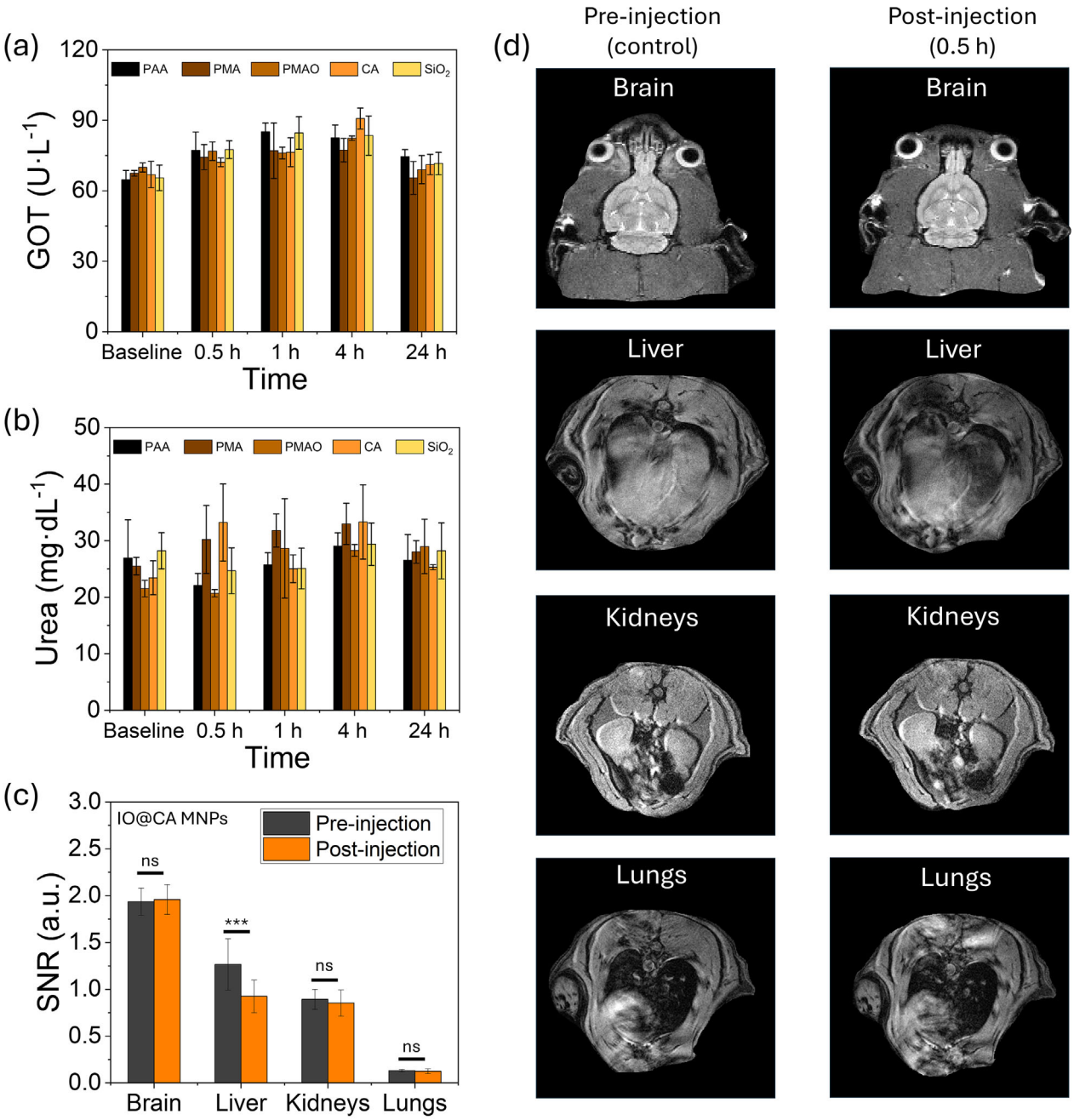

FIGURE 5 | (a) GOT and (b) urea levels measured pre-injection (baseline) and 0.5, 1, 4, and 24 h after intravenous administration of ligand-functionalized T_2 contrast agents (1 mL, 2.5 mM Fe) in Sprague–Dawley rats. (c) SNR in the brain, liver, kidneys, and lungs from in vivo studies before and post-injection (0.5 h) of CA-functionalized T_2 contrast agents, quantified from MR images relative to muscle signal. (d) Representative T_2-weighted MR images of the brain and body organs–including liver, kidneys, and lungs–acquired before (left panels) and after (right panels) CA-functionalized nanoparticle injection. Data are shown as mean ± SD ($n = 3$). Statistical significance is indicated by asterisks (*$p < 0.05$, **$p < 0.01$, ***$p < 0.001$; ns, not significant).

The T_2 and T_2* signal reductions observed in vivo under UHF conditions were consistent with the trends seen in phantom studies, although the extent of attenuation better aligned with a lower concentration of 0.04 mM. This suggests that the actual effective dose reaching brain tissue is substantially lower than the nominal injected concentration, likely due to limited diffusion, tissue interactions, or partial loss during administration. Importantly, despite these biological limitations, the contrast efficiency hierarchy across ligands remained largely preserved in vivo. Formulations such as IO@PAA, IO@CA, and IO@PMAO consistently produced stronger T_2 and T_2* attenuation, validating the predictive value of ligand-driven optimization. Moreover, after intravenous injections in Sprague–Dawley rats, the contrast agents showed no significant hepatic or renal toxicity, and CA-functionalized T_2 MNPs accumulated mainly in the liver and, to a lesser extent, in the kidneys. These results demonstrate that rational surface chemistry tuning translates into meaningful differences in biological performance, and that in vitro

screening can reliably guide the design of iron oxide-based T_2 contrast agents for complex physiological environments. In particular, this work highlights ligand engineering as a simple and cost-effective strategy to modulate T_2 efficiency. Among the systems studied, CA-based contrast agents show strong potential for MRI, combining high r_2 relaxivity with a favorable short-term safety profile. Further studies addressing long-term biodistribution and toxicity will be essential to support their clinical translation.

4 | Materials and Methods

4.1 | Synthesis of Iron Oxide Nanoparticles in Organic Media (IO@OA)

The synthesis of precursor hydrophobic iron oxide NPs (d_{TEM} = 12.2 ± 1.6 nm) denoted as IO@OA, was carried out following the thermal decomposition method previously described with slight modifications [89]. Initially, iron acetylacetonate (2.119 g), 1,2-hexadecanediol (6.203 g), oleic acid (4.460 g), and oleylamine (3.209 g) were dissolved in benzyl ether (40 mL) at 110°C for 60 min with mechanical stirring at 400 rpm under vacuum. Subsequently, under a flow of nitrogen and reflux conditions, the temperature increased at a rate of 8°C/min to reach 210°C, where it was maintained for 2 h. Then, the temperature was further increased to 300°C following a heating ramp of 5°C/min and held for 1 h. Finally, the reaction was allowed to cool to room temperature. After cooling, the MNPs were precipitated by adding 50 mL of ethanol, followed by a centrifugation process. The resulting black precipitate was resuspended in a mixture of 50 mL of toluene and 500 µL of OA and OAm. Subsequently, the solution was centrifuged, the precipitate was discarded to eliminate possible aggregates, and the supernatant was recovered and redispersed in 50 mL of ethanol. Finally, the solution was centrifuged again, and the precipitate was resuspended in an organic medium (cyclohexane).

4.2 | Transfer to Aqueous Media

As a result of thermal decomposition conditions, the samples obtained exhibit hydrophobic characteristics and required a ligand exchange modification to ensure stable transfer to aqueous media. Various compounds were utilized, namely PAA, PMA, PMAO, CA, and SiO_2, and the samples were accordingly named by IO@X, where X represents the coating employed (X = PAA, PMA, PMAO, CA, or SiO_2).

4.2.1 | Phase Transfer by Ligand-Exchange with PAA

The sets of MNPs transferred to the aqueous medium using PAA as the ligand (IO@PAA) were synthesized according to a previously reported method [47]. Briefly, 1 mL (C = 5 mg mL^{-1}) of IO@OA MNPs dispersed in cyclohexane was transferred into a solution of PAA (11.5 mg) in 50 mL of dimethyl sulfoxide. The amount of PAA employed was adjusted based on a molar ratio of the exchange ligand-to-NP surface Fe atoms at 5:1. The mixture was subjected to magnetic stirring for 48 h at 700 rpm. Finally, the MNPs were precipitated by centrifugation (14 000 rpm, 30 min) and redispersed in H_2O.

4.2.2 | Phase Transfer by Ligand-Exchange with PMA

The sets of MNPs transferred to aqueous medium employed and utilizing PMA as the ligand (IO@PMA) were synthesized following previously reported work [89]. Initially, a dodecylamine-modified PMA polymer with amphiphilic character must be synthesized. For this purpose, a specified amount of PMA (3.084 g) was placed in a round flask, and a solution of dodecylamine (15 mmol) in tetrahydrofuran (100 mL) was rapidly injected into the flask. The solution was vigorously mixed by sonication and maintained at 60°C under vigorous stirring (700 rpm) overnight. Subsequently, the solvent was evaporated using a rotary evaporator (200 rpm, 45°C, and 450 mbar) until complete solvent removal. The resulting dried polymer was redispersed in anhydrous chloroform (25 mL), adjusting the final concentration to 0.8 M. The transfer to an aqueous medium of IO@OA MNPs was performed by mixing the previously synthesized dodecylamine-modified PMA polymer (2.2 mL, 0.8 M) and IO@OA MNPs (15 mg) both in organic medium (chloroform). The respective quantities were adjusted to a ratio $X = 400$ nm^{-2}, where X represents the number of PMA monomers added per effective MNP surface unit area (detailed calculations are provided in [89]). Subsequently, a rotary evaporation process (45 min at 200 rpm, 45°C and 450 mbar) was employed to evaporate the solvent, and the resulting solid was redispersed in chloroform (30 mL). This process needed to be repeated at least two more times to ensure the proper functionalization of the MNPs. The solid sample was dissolved in sodium borate buffer (50 mM, pH 12) under sonication and vigorous stirring until the MNPs were thoroughly dispersed in the medium. The resulting solution was concentrated through centrifugal filtration using a 100 kDa cut-off filter at 2000 rpm, collected, and transferred to milli-Q water. Finally, the excess polymer was removed by centrifugation at 13 300 rpm for 2 h, repeating the process at least 3 times.

4.2.3 | Phase Transfer by Ligand-Exchange with PMAO

The sets of MNPs transferred to the aqueous medium, using PMAO as the ligand (IO@PMAO), were synthesized following a previously reported procedure [90]. Briefly, 20 mg of IO@OA (in powder state), were added to a solution of PMAO (250 mg) dissolved in chloroform (200 mL) and stirred magnetically (1 h, 25°C) until fully dissolved. The solvent was then removed under vacuum, and a small amount of chloroform (1 mL) was added to the dried MNPs. To facilitate the transfer to water, the MNPs were first resuspended in NaOH solution (0.05 M), and the chloroform present in the solution was evaporated by magnetic stirring at T = 60°C. The resulting solution was concentrated using centrifugal filtration with a 100 kDa cut-off filter at 2000 rpm, collected, and transferred to milli-Q water. Finally, the excess polymer was removed by centrifugation at 13 300 rpm for 2 h, repeating the process at least 3 times.

4.2.4 | Phase Transfer by Ligand-Exchange with Citric Acid

The sets of MNPs transferred to aqueous medium, utilizing CA as the ligand (IO@CA) were synthesized following a previously reported work [45]. IO@OA (15 mg) were first dried and dispersed in a 50:50 mixture of 1,2-dichlorobenzene (7.5 mL) and *N*, *N*′-dimethylformamide (7.5 mL), to which CA (100 mg) was added. The solution was magnetically stirred (18 h, 100°C) under reflux and vacuum to prevent the oxidation of MNPs. Subsequently, diethyl ether (40 mL) was added, and the MNPs were collected using a permanent magnet. The obtained MNPs underwent several washes with acetone and were precipitated by centrifugation (13 300 rpm, 30 min). Finally, the MNPs were filtered through a membrane pore filter (0.1 μm) and redispersed in milli-Q water.

4.2.5 | Phase Transfer by Ligand-Exchange with SiO_2

The sets of MNPs transferred to the aqueous medium, employed SiO_2 as an inorganic shell (IO@SiO_2), were synthesized through the microemulsion method as described in previous works [91, 92]. Initially, IGEPAL CO-520 (1.88 g) were dissolved in cyclohexane (24 mL) under mechanical stirring (350 rpm, 30 min). Subsequently, IO@OA (10 mg) dispersed in cyclohexane were added to the mixture and subjected to mechanical stirring (350 rpm, 30 min). The corresponding amounts of NH_4OH (0.175 mL) and tetraethyl orthosilicate (0.16 mL) were incorporated, and the mixture was mechanically stirred (350 rpm, 16 h), ensuring protection from solar radiation and light sources. Finally, the corresponding amount of 2-propanol was added until flocculation of the MNPs was observed. The MNPs were then retained using a permanent magnet, and the supernatant was discarded. This procedure was repeated successively using a 1:1 mixture of 2-propanol-ethanol, ethanol, and a 1:1 mixture of ethanol: H_2O. Finally, the MNPs were washed twice with H_2O and centrifuged (9000 rpm, 30 min), redispersing the pellet in H_2O.

4.3 | Physicochemical Characterization of Iron Oxide-Based T_2-Contrast Agents

The characterization of MNPs crystalline phases was carried out through X-ray diffraction (XRD) on powdered samples using a Philips PW1710 diffractometer (Cu K_a radiation source, λ = 1.54 186 Å). Measurements were collected in a 2θ-angle range between 10° and 80° with steps of 0.02° and a duration of 10 s per step. The morphology of the MNPs was assessed by transmission electron microscopy (TEM) using a JEOL JEM-1011 microscope (100 kV). Sample preparation involved depositing 7 μL of dispersed MNPs onto a carbon-coated Cu grid, followed by solvent evaporation at room temperature. The Fe concentration was determined using inductively coupled plasma emission spectroscopy (ICP-OES, ICPE-9000 Multitype ICP Emission Spectrometer, Shimadzu). Sample preparation included digesting approximately 10–20 μL of MNPs in 1 mL of HCl (37% v/v) overnight, followed by dilution with Milli-Q water (10 mL total volume). The composition of the samples in powder state was analyzed using a TGA Perkin Elmer model 7 (Perkin Elmer, Waltham, MA, USA). DC magnetization curves of MNPs were measured using a Quantum Design superconducting quantum interference device (SQUID) magnetometer (Quantum Design, Darmstadt, Germany). Approximately 1 mg of powdered MNPs was placed in gelatin capsules. Zero-field-cooled (ZFC) and field-cooled (FC) curves were recorded at an applied magnetic field of 100 Oe within the temperature range of 10 to 350 K. Hysteresis loops were measured with an applied magnetic field between −25 and 25 KOe at 300 K.

4.4 | In Vitro MR Relaxometry (B_0 = 1.4 T)

Relaxation performance of iron oxide-based T_2- contrast agents with Fe concentrations ranging from 0 and 0.8 mM was measured using a Minispec benchtop relaxometer (mq 60, Bruker, B_0 = 1.41 T) operating at 60 MHz and conducted at a temperature of 37°C. T_2 (s) were measured using a standard Carr–Purcell–Meiboom–Gill (CPMG) sequence and from these measurements, r_2 were determined.

4.5 | In Vitro MR Imaging (B_0 = 3 T)

MR imaging was performed using a 3 T horizontal bore MR Solutions Benchtop scanner equipped with 48 G cm^{-1} actively shielded gradients. To image the MNPs, a 56 mm diameter quadrature bird-cage coil was used in transmit/receive mode. MRI phantom samples were prepared dispersing MNPs with different Fe concentrations ranging from 0 to 100 μM in H_2O. Approximately 100 μL of each MNP was placed on a custom-printed PLA well plate, positioned at the center of the coil. T_2-weighted images were acquired using the fast spin echo (FSE) sequence with the following parameters: Echo time (TE) = 11-110 ms, repetition time (TR) = 4 000 ms, number of averages (NA) = 32. MRI images of phantoms were acquired with an image matrix of 256 × 256, a field of view (FOV) of 6 × 6 cm^2, six slices with a slice thickness of 0.5 mm, and a slice gap of 0 mm.

4.6 | In Vitro MR Imaging (B_0 = 9.4 T)

MR imaging was performed using a 9.4 T horizontal bore magnet (Bruker BioSpin) equipped with 12-cm actively shielded gradient coils (440 mT m^{-1}). MRI phantom samples were prepared dispersing MNPs in an agar (1.6% w/v) mold with multiple wells, following a procedure described elsewhere [93]. MNPs were first diluted in water to obtain Fe concentrations ranging from 0 to 100 μM, then mixed with liquid agar (70°C) and placed in the solid agar mold. The mold was then sealed with liquid agar and cooled to room temperature. T_2-weighted images were acquired using the multi-slice multi-spin-echo (MSME) sequence with TE = 11.32 ms, TR = 3000 ms, 16 echoes with echo spacing (ES) = 11.32 ms, 50 kHz spectral bandwidth (SB), a flip angle (FA) of 90°, 14 slices of 1 mm, and NA = 1. Images were obtained with a FOV of 7.5 × 7.5 cm^2 (with saturation bands to suppress signals outside this FOV) and a matrix size of 300 × 300, giving an in-plane resolution of 250 μm/pixel and implemented without fat suppression.

4.7 | In Vivo Studies

The studies followed the ARRIVE guidelines (Animal Research: Reporting In Vivo Experiments). The use of animals in this study was approved by the Animal Research and Welfare Ethics Committee of the Health Research Institute of Santiago de Compostela (IDIS; Santiago de Compostela, Spain) and was authorized under procedure number 15011/2025/002 by the Farming and Ranching Agency of the Xunta de Galicia (Regional Government, Spain), in accordance with European (Council Directive 2010/63/EU) and Spanish regulations (RD 53/2013). Online software (Experimental Design Assistant; https://eda.nc3rs.org.uk/eda/login/auth) was used for sample size calculation and animal randomization. Eighteen (n = 18) male Sprague–Dawley rats [7 weeks old, 239 ± 13 g; Experimental Biomedicine Centre (CEBEGA), University of Santiago de Compostela] were used. The rats were housed in pairs in cages with enriched cardboard material. Animals were kept in a controlled environment at 22°C ± 1°C and 60% ± 5% humidity, with 12:12 h light: dark cycles, and had free access to standard food and water for one week prior to the surgical procedure. The animals were randomly divided into a control group (uninjected, $n = 3$) and five different nanoparticle-treated groups ($n = 3$ each).

4.8 | In Vivo Brain MRI

To perform brain MRI imaging, iron oxide-based T_2 contrast agents and PBS were directly injected into the brain parenchyma of the animals (n = 3, 0.5 mM Fe) under anesthesia. In brief, the Hamilton syringe was filled with the respective nanoparticle suspension, and 10 µL of MNPs suspension was administered into the right hemisphere of the brain at a flow rate of 1 µL/min over a 10-minute period. The same procedure was applied to the left hemisphere, where 10 µL of PBS was injected. Following surgery, MRI scans were performed using a 9.4 T horizontal-bore magnet (Bruker BioSpin) equipped with 12-cm actively shielded gradient coils (440 mT/m). Signal transmission was carried out using a linear birdcage resonator (7 cm in diameter), while signal detection was performed using a 2 × 2 surface coil array positioned over the animal's head, which was secured with a bite bar, earplugs, and adhesive tape. The transmission and reception coils were actively decoupled. Gradient-echo pilot scans were first conducted in each imaging session to ensure accurate positioning of the animal within the magnet bore. Animals were included in the study if nanoparticles were detected in the correct brain area by MRI and were excluded if a blood vessel was severely damaged during surgery. All surgeries were performed by the same researcher.

To evaluate the in vivo presence of MNPs, MRI scans were conducted using T_2-weighted and T_2*-weighted sequences. T_2*-weighted images were acquired with an multi-gradient echo (MGE) sequence using a TE = 2.9 ms, TR = 1500 ms, 16 echoes with ES = 3.28 ms, FA = 30°, NA = 2, and 14 slices of 1 mm thickness. The FOV was 19.2 × 19.2 mm^2, with a 192 × 192 image matrix, providing an isotropic in-plane resolution of 100 µm per pixel. T_2-weighted images were obtained with a rapid acquisition with relaxation enhancement (RARE) T_2 sequence, featuring an TE = 11 ms, RARE factor of 8, TR = 2500 ms, NA = 2, 1 repetition, FA = 90°, 14 slices of 1 mm thickness, a 26 × 26 mm^2 FOV, and a matrix size of 256 × 256, maintaining an isotropic in-plane resolution of 100 µm per pixel. Fat suppression was not applied. MRI post-processing was performed using ImageJ software (W. Rasband, NIH, USA).

4.9 | Calculation of SNR and CNR in Rat Brain ROIs

Quantitative analysis of the in vivo MR images was performed by calculating SNR and CNR. ROIs were manually defined in the injected brain area and in the contralateral hemisphere injected with PBS, while background noise was estimated from a signal-free region outside the animal. SNR was calculated as the ratio between the mean signal intensity within the injected ROI and the standard deviation of the background noise. CNR was calculated as the absolute difference between the mean signal intensities of the injected and contralateral ROIs, normalized to the background noise standard deviation.

4.10 | In Vivo Biocompatibility of Iron Oxide-Based T_2-Contrast Agents

The biocompatibility of the MNPs in vivo was evaluated by monitoring serum levels of GOT, urea, and creatinine after intravenous injection via the tail vein in anesthetized rats (1 mL, 2.5 mM Fe, n = 3). A matching volume of PBS served as the control. Blood samples were collected at 0 (baseline), 0.5, 1, 4, and 24 h post-injection, using heparinized collection tubes (BD Vacutainer Heparin). For analysis, 32 µL of blood were applied to reagent strips to determine GOT, urea, and creatinine levels, which were measured with a Reflotron Plus system (Roche, Basel, Switzerland).

4.11 | In Vivo Biodistribution of Iron Oxide-Based T_2-Contrast Agents

Biodistribution was evaluated by magnetic resonance imaging by acquiring T_2-weighted images before and after intravenous administration of CA-functionalized contrast agents (1 mL, 2.5 mM Fe) in Sprague–Dawley rats, without removing the animal from the magnet. T_2-weighted images were obtained using a RARE sequence with TE = 20 ms, TR = 906 ms, RARE factor of 4, NA = 4, SB = 50 kHz, and FA = 90°. Thirty-five coronal or sixteen axial slices were acquired for body or brain studies, respectively, with a slice thickness of 1–2 mm. Imaging was performed using a FOV of 7 × 7 cm^2 (body) and 8 × 6 cm^2 (brain), with saturation bands applied to suppress signals from outside the selected imaging volume. Images were reconstructed using matrix sizes of 256 × 256 (body) and 384 × 192 (brain), yielding in-plane spatial resolutions of 273 × 273 µm^2 (body) and 208 × 312 µm^2 (brain). No fat suppression was applied. T_2 signal intensities (arbitrary units) for each organ were quantified by comparing pre- and post-injection images relative to the surrounding tissue.

4.12 | Statistical Analysis

All statistical analyses were conducted with OriginPro 2016 (OriginLab Corporation, Northampton, MA, USA). Particle size distributions derived from TEM images were processed using ImageJ and reported as mean ± SD. Furthermore, the Distribution Fit function in OriginPro was utilized to evaluate the fit quality of the size distributions. Hydrodynamic diameter, ζ-potential, and iron content measurements were performed in triplicate ($n = 3$) and are presented as mean ± SD. Statistical significance was determined using a two-sample Student's t-test comparing pre-injection (control) and post-injection groups. Levels of statistical significance are indicated by asterisks ($p < 0.05$, $^*p < 0.01$, $p < 0.001$; ns, not significant).

Acknowledgements

This work was supported by CARTsol project (PLEC2022-009217 funded by MICINN/AEI /10.13039/ 501100011033 and NextGenerationEU/ PRTR). P. García-Acevedo thanks to Axencia Galega de Innovación (Spain) for his Posdoctoral Grant (Axudas de apoio á etapa de formación posdoutoral – IN606B-2024.1). R. Iglesias-Rey (CP22/00061) from the Miguel Servet Program of Instituto de Salud Carlos III and Co-financed by the EU.

Conflicts of Interest

The authors declare no conflict of interest.

Data Availability Statement

The data that support the findings of this study are available from the corresponding author upon reasonable request.

References

1. Z. Zhou, L. Yang, J. Gao, and X. Chen, "Structure–Relaxivity Relationships of Magnetic Nanoparticles for Magnetic Resonance Imaging," *Advanced Materials* 31 (2019): 1804567, https://doi.org/10.1002/adma.201804567.

2. M. Jeon, M. V. Halbert, Z. R. Stephen, and M. Zhang, "Iron Oxide Nanoparticles as T1 Contrast Agents for Magnetic Resonance Imaging: Fundamentals, Challenges, Applications, and Prospectives," *Advanced Materials* 33 (2021): 1906539, https://doi.org/10.1002/adma.201906539.

3. E. Terreno, D. D. Castelli, A. Viale, and S. Aime, "Challenges for Molecular Magnetic Resonance Imaging," *Chemical Reviews* 110 (2010): 3019–3042.

4. J. Estelrich, M. J. Sánchez-Martín, and M. A. Busquets, "Nanoparticles in Magnetic Resonance Imaging: From Simple to Dual Contrast Agents," *International Journal of Nanomedicine* 10 (2015): 1727–1741.

5. H. Du, Q. Wang, B. Zhang, et al., "Structural Defect-Enabled Magnetic Neutrality Nanoprobes for Ultra-High-Field Magnetic Resonance Imaging of Isolated Tumor Cells In Vivo," *Advanced Materials* 36 (2024): 2401538, https://doi.org/10.1002/adma.202401538.

6. Z. Fei, Y. Zhang, S. Ni, et al., "Spin-State Modulation of Iron Oxide Nanoparticles via Cobalt(III) Engineering Enables Precision MRI Contrast at Ultra-High-Field," *Small* (2025): 10590, https://doi.org/10.1002/smll.202510590.

7. D. A. Feinberg, A. J. S. Beckett, A. T. Vu, et al., "Next-Generation MRI Scanner Designed for Ultra-High-Resolution Human Brain Imaging at 7 Tesla," *Nature Methods* 20 (2023): 2048–2057.

8. J. Nowogrodzki, "The World's Strongest MRI Machines Are Pushing Human Imaging to New Limits," *Nature* 563 (2018): 24–26, https://doi.org/10.1038/d41586-018-07182-7.

9. O. Kraff, A. Fischer, A. M. Nagel, C. Mönninghoff, and M. E. Ladd, "MRI at 7 Tesla and Above: Demonstrated and Potential Capabilities," *Journal of Magnetic Resonance Imaging* 41 (2015): 13–33.

10. Z. Liang, Q. Wang, H. Liao, et al., "Artificially Engineered Antiferromagnetic Nanoprobes for Ultra-Sensitive Histopathological Level Magnetic Resonance Imaging," *Nature Communications* 12 (2021): 3840 , https://doi.org/10.1038/s41467-021-24055-2.

11. A. Banerjee, B. Blasiak, A. Dash, B. Tomanek, F. C. J. M. van Veggel, and S. Trudel, "High-Field Magnetic Resonance Imaging: Challenges, Advantages, and Opportunities for Novel Contrast Agents," *Chemical Physics Reviews* 3 (2022): 011304 , https://doi.org/10.1063/5.0064517.

12. United States Food and Drug Administration, "FDA clears first 7T magnetic resonance imaging device" (2017, October 12), https://www.fda.gov/news-events/press-announcements/fda-clears-first-7t-magnetic-resonance-imaging-device.

13. N. Lee and T. Hyeon, "Designed Synthesis of Uniformly Sized Iron Oxide Nanoparticles for Efficient Magnetic Resonance Imaging Contrast Agents," *Chemical Society Reviews* 41 (2012): 2575–2589.

14. D. Ni, W. Bu, E. B. Ehlerding, W. Cai, and J. Shi, "Engineering of Inorganic Nanoparticles as Magnetic Resonance Imaging Contrast Agents," *Chemical Society Reviews* 46 (2017): 7438–7468.

15. J. Yang, J. Feng, S. Yang, Y. Xu, and Z. Shen, "Exceedingly Small Magnetic Iron Oxide Nanoparticles for T1-Weighted Magnetic Resonance Imaging and Imaging-Guided Therapy of Tumors," *Small* 19 (2023): 2302856, https://doi.org/10.1002/smll.202302856.

16. M. O. Besenhard, L. Panariello, C. Kiefer, et al., "Small Iron Oxide Nanoparticles as MRI T1 Contrast Agent: Scalable Inexpensive Water-Based Synthesis Using a Flow Reactor," *Nanoscale* 13 (2021): 8795–8805.

17. Y. Cao, Z. Mao, Y. He, et al., "Extremely Small Iron Oxide Nanoparticle-Encapsulated Nanogels as a Glutathione-Responsive T1 Contrast Agent for Tumor-Targeted Magnetic Resonance Imaging," *ACS Applied Materials & Interfaces* 12 (2020): 26973–26981.

18. Y. Bao, J. A. Sherwood, and Z. Sun, "Magnetic Iron Oxide Nanoparticles as T1 Contrast Agents for Magnetic Resonance Imaging," *Journal of Materials Chemistry C* 6 (2018): 1280–1290.

19. H. Zhou, X. Lu, C. Du, et al., "Cycloacceleration of Reactive Oxygen Species Generation Based on Exceedingly Small Magnetic Iron Oxide Nanoparticles for Tumor Ferroptosis Therapy," *Small* 18 (2022): 2202705, https://doi.org/10.1002/smll.202202705.

20. Y. Huang, W. Xiong, X. Qin, et al., "Large-Scale Synthesis of Biodegradable Iron-Based Contrast Agent for High Performance T1-Weighted Magnetic Resonance Imaging," *Chemical Engineering Journal* 509 (2025): 161263, https://doi.org/10.1016/j.cej.2025.161263.

21. X. Lu, H. Zhou, Z. Liang, et al., "Biodegradable and Biocompatible Exceedingly Small Magnetic Iron Oxide Nanoparticles for T1-Weighted Magnetic Resonance Imaging of Tumors," *Journal of Nanobiotechnology* 20 (2022): 350, https://doi.org/10.1186/s12951-022-01562-y.

22. Z. Shen, T. Chen, X. Ma, et al., "Multifunctional Theranostic Nanoparticles Based on Exceedingly Small Magnetic Iron Oxide Nanoparticles for T1-Weighted Magnetic Resonance Imaging and Chemotherapy," *ACS Nano* 11 (2017): 10992–11004.

23. J. Jose, R. Kumar, S. Harilal, et al., "Magnetic Nanoparticles for Hyperthermia in Cancer Treatment: An Emerging Tool," *Environmental Science and Pollution Research* 27 (2020): 19214–19225.

24. B. E. Kashevsky, S. B. Kashevsky, T. I. Terpinskaya, and V. S. Ulashchik, "Magnetic Hyperthermia with Hard-Magnetic Nanoparticles: In Vivo Feasibility of Clinically Relevant Chemically Enhanced Tumor Ablation," *Journal of Magnetism and Magnetic Materials* 475 (2019): 216–222.

25. A. A. Demessie, Y. Park, P. Singh, et al., "An Advanced Thermal Decomposition Method to Produce Magnetic Nanoparticles with Ultra-high Heating Efficiency for Systemic Magnetic Hyperthermia," *Small Methods* 6 (2022): 2200916, https://doi.org/10.1002/smtd.202200916.

26. Y. Zhang, X. Fu, J. Jia, et al., "Glioblastoma Therapy Using Codelivery of Cisplatin and Glutathione Peroxidase Targeting siRNA From Iron Oxide Nanoparticles," *ACS Applied Materials & Interfaces* 12 (2020): 43408–43421.

27. M. Ribeiro, M. Boudoukhani, E. Belmonte-Reche, et al., "Xanthan-Fe3O4 Nanoparticle Composite Hydrogels for Non-Invasive Magnetic Resonance Imaging and Magnetically Assisted Drug Delivery," *ACS Applied Nano Materials* 4 (2021): 7712–7729.

28. A. Pourjavadi, M. Kohestanian, and C. Streb, "pH and Thermal Dual-Responsive Poly(NIPAM-co-GMA)-Coated Magnetic Nanoparticles via Surface-Initiated RAFT Polymerization for Controlled Drug Delivery," *Materials Science and Engineering: C* 108 (2020): 110418, https://doi.org/10.1016/j.msec.2019.110418.

29. C. Lu, L. Han, J. Wang, J. Wan, G. Song, and J. Rao, "Engineering of Magnetic Nanoparticles as Magnetic Particle Imaging Tracers," *Chemical Society Reviews* 50 (2021): 8102–8146.

30. J. Wang, Y. Jia, Q. Wang, et al., "An Ultrahigh-Field-Tailored T1–T2 Dual-Mode MRI Contrast Agent for High-Performance Vascular Imaging," *Advanced Materials* 33 (2021): 2004917, https://doi.org/10.1002/adma.202004917.

31. B. Vachha and S. Y. Huang, "MRI with Ultrahigh Field Strength and High-Performance Gradients: Challenges and Opportunities for Clinical Neuroimaging at 7 T and Beyond," *European Radiology Experimental* 5 (2021): 35, https://doi.org/10.1186/s41747-021-00216-2.

32. A. G. Van Der Kolk, J. Hendrikse, J. J. M. Zwanenburg, F. Visser, and P. R. Luijten, "Clinical Applications of 7T MRI in the Brain," *European Journal of Radiology* 82 (2013): 708–718.

33. H. Du, Q. Wang, Z. Liang, Q. Li, F. Li, and D. Ling, "Fabrication of Magnetic Nanoprobes for Ultrahigh-Field Magnetic Resonance Imaging," *Nanoscale* 14 (2022): 17483–17499.

34. S. Laurent, D. Forge, M. Port, et al., "Magnetic Iron Oxide Nanoparticles: Synthesis, Stabilization, Vectorization, Physicochemical Characterizations, and Biological Applications," *Chemical Reviews* 108 (2008): 2064–2110.

35. H. Lu, A. Chen, X. Zhang, et al., "A pH-Responsive T1-T2 Dual-Modal MRI Contrast Agent for Cancer Imaging," *Nature Communications* 13 (2022): 7948 , https://doi.org/10.1038/s41467-022-35655-x.

36. J. S. Choi, S. Kim, D. Yoo, et al., "Distance-Dependent Magnetic Resonance Tuning as a Versatile MRI Sensing Platform for Biological Targets," *Nature Materials* 16 (2017): 537–542.

37. Z. Zhou, R. Bai, J. Munasinghe, Z. Shen, L. Nie, and X. Chen, "T1–T2 Dual-Modal Magnetic Resonance Imaging: From Molecular Basis to Contrast Agents," *ACS Nano* 11 (2017): 5227–5232.

38. Q. Xie, X. Wang, G. Zhang, et al., "Ultrasmall Fe3O4 Nanoparticles Self-Assembly Induced Dual-Mode T1/T2-Weighted Magnetic Resonance Imaging and Enhanced Tumor Synergetic Theranostics," *Scientific Reports* 14 (2024): 10646 , https://doi.org/10.1038/s41598-024-59525-2.

39. Q. Cheng, Y. Chang, D. Zhang, et al., "Biomineralization Synthesis of HoMn Nanoparticles for Ultrahigh-Field-Tailored and T1–T2 Dual-Mode MRI-Guided Cancer Theranostics," *ACS Nano* 18 (2024): 27853–27868, https://doi.org/10.1021/acsnano.4c00516.

40. Y. Liu, S. L. Ho, T. Tegafaw, et al., "Clustered Ultra-Small Iron Oxide Nanoparticles as Potential T1/T2 Dual–Modal Magnetic Resonance Imaging Contrast Agents and Application to Tumor Model," *Nanotechnology* 35 (2024): 505101, https://doi.org/10.1088/1361-6528/ad8203.

41. Z. Zhou, R. Tian, Z. Wang, et al., "Artificial Local Magnetic Field Inhomogeneity Enhances T2 Relaxivity," *Nature Communications* 8 (2017): 15468, https://doi.org/10.1038/ncomms15468.

42. M. D. Yang, C. H. Ho, S. Ruta, et al., "Magnetic Interaction of Multifunctional Core–Shell Nanoparticles for Highly Effective Theranostics," *Advanced Materials* 30 (2018): 1802444, https://doi.org/10.1002/adma.201802444.

43. P. Dong, T. Zhang, H. Xiang, et al., "Controllable Synthesis of Exceptionally Small-Sized Superparamagnetic Magnetite Nanoparticles for ultrasensitive MR Imaging and Angiography," *Journal of Materials Chemistry B* 9 (2021): 958–968.

44. V. Patsula, D. Horák, J. Kučka, et al., "Synthesis and Modification of Uniform PEG-Neridronate-Modified Magnetic Nanoparticles Determines Prolonged Blood Circulation and Biodistribution in a Mouse Preclinical Model," *Scientific Reports* 9 (2019): 10765, https://doi.org/10.1038/s41598-019-47262-w.

45. S. I. C. J. Palma, M. Marciello, A. Carvalho, S. Veintemillas-Verdaguer, M. P. del Morales, and A. C. A. Roque, "Effects of Phase Transfer Ligands on Monodisperse Iron Oxide Magnetic Nanoparticles," *Journal of Colloid and Interface Science* 437 (2015): 147–155.

46. H. Duan, M. Kuang, X. Wang, Y. A. Wang, H. Mao, and S. Nie, "Reexamining the Effects of Particle Size and Surface Chemistry on the Magnetic Properties of Iron Oxide Nanocrystals: New Insights into Spin Disorder and Proton Relaxivity," *The Journal of Physical Chemistry C* 112 (2008): 8127–8131.

47. Y. Xu, Y. Qin, S. Palchoudhury, and Y. Bao, "Water-Soluble Iron Oxide Nanoparticles with High Stability and Selective Surface Functionality," *Langmuir* 27 (2011): 8990–8997.

48. J. Ge, C. Li, N. Wang, et al., "Effects of PEG Chain Length on Relaxometric Properties of Iron Oxide Nanoparticles-Based MRI Contrast Agent," *Nanomaterials* 12 (2022): 2673, https://doi.org/10.3390/nano12152673.

49. M. Cho, J. Villanova, D. M. Ines, et al., "Sensitive T2 MRI Contrast Agents from the Rational Design of Iron Oxide Nanoparticle Surface Coatings," *The Journal of Physical Chemistry C* 127 (2023): 1057–1070.

50. F. Brero, P. Arosio, M. Albino, et al., "1H-NMR Relaxation of Ferrite Core-Shell Nanoparticles: Evaluation of the Coating Effect," *Nanomaterials* 13 (2023): 804, https://doi.org/10.3390/nano13050804.

51. Z. Liang, L. Xiao, Q. Wang, et al., "Ligand-Mediated Magnetism-Conversion Nanoprobes for Activatable Ultra-High Field Magnetic Resonance Imaging," *Angewandte Chemie International Edition* 63 (2024): 202318948, https://doi.org/10.1002/anie.202318948.

52. Z. Lu, J. Yan, M. Xu, et al., "A "Dual-Key-and-Lock" MRI Contrast Agent with T1 –T2 Switchable Function for Accurate Diagnosis of Tumors," *Nano Letters* 24 (2024): 9406–9414.

53. X. Liu, Z. Liang, H. Du, et al., "DNA-Mediated Magnetic-Dimer Assembly for Fault-Free Ultra-High-Field Magnetic Resonance Imaging of Tumors," *Nano Letters* 24 (2024): 6696–6705.

54. L. M. Sanchez, D. A. Martin, V. A. Alvarez, and J. S. Gonzalez, "Polyacrylic Acid-Coated Iron Oxide Magnetic Nanoparticles: The Polymer Molecular Weight Influence," *Colloids and Surfaces A: Physicochemical and Engineering Aspects* 543 (2018): 28–37.

55. S. L. C. Pinho, G. A. Pereira, P. Voisin, et al., "Fine Tuning of the Relaxometry of γ-Fe2O3 @SiO2 Nanoparticles by Tweaking the Silica Coating Thickness," *ACS Nano* 4 (2010): 5339–5349.

56. N. Van Khien, C. Thi Anh Xuan, L. H. Nguyen, P. H. Nam, and T. T. Thao, "Role of Citric Acid Coating in Enhancing Applicability of CoFe2O4 Nanoparticles in Antibacterial and Hyperthermia," *Materials Today Communications* 38 (2024): 107982, https://doi.org/10.1016/j.mtcomm.2023.107982.

57. N. Thi Thuy Khue, L. T. Thanh Tam, N. Thanh Dung, et al., "Water-Dispersible Gadolinium Oxide Nanoplates as an Effective Positive Magnetic Resonance Imaging Contrast Agent," *ChemistrySelect* 7 (2022): 202202062, https://doi.org/10.1002/slct.202202062.

58. M. Ajdary, F. Keyhanfar, M. A. Moosavi, R. Shabani, M. Mehdizadeh, and R. S. Varma, "Potential Toxicity of Nanoparticles on the Reproductive System Animal Models: A Review," *Journal of Reproductive Immunology* 148 (2021): 103384, https://doi.org/10.1016/j.jri.2021.103384.

59. V. Zavisova, M. Koneracka, A. Gabelova, et al., "Effect of Magnetic Nanoparticles Coating on Cell Proliferation and Uptake," *Journal of Magnetism and Magnetic Materials* 472 (2019): 66–73.

60. M. Zheng, J. Lu, and D. Zhao, "Effects of Starch-Coating of Magnetite Nanoparticles on Cellular Uptake, Toxicity and Gene Expression Profiles in Adult Zebrafish," *Science of The Total Environment* 622–623 (2018): 930–941.

61. M. G. Bekaroğlu, A. Alemdar, and S. İşçi, "Comparison of Ionic Polymers in the Targeted Drug Delivery Applications as the Coating Materials on the Fe3O4 Nanoparticles," *Materials Science and Engineering: C* 103 (2019): 109838, https://doi.org/10.1016/j.msec.2019.109838.

62. C. Turrina, A. Klassen, D. Milani, et al., "Superparamagnetic Iron Oxide Nanoparticles for Their Application in the Human Body: Influence of the Surface," *Heliyon* 9 (2023): 16487, https://doi.org/10.1016/j.heliyon.2023.e16487.

63. Y. Liu, Q. Xia, Y. Liu, et al., "Genotoxicity Assessment of Magnetic Iron Oxide Nanoparticles with Different Particle Sizes and Surface Coatings," *Nanotechnology* 25 (2014): 425101, https://doi.org/10.1088/0957-4484/25/42/425101.

64. K. R. Di Bona, Y. Xu, P. A. Ramirez, et al., "Surface Charge and Dosage Dependent Potential Developmental Toxicity and Biodistribution of Iron Oxide Nanoparticles in Pregnant CD-1 Mice," *Reproductive Toxicology* 50 (2014): 36–42.

65. S. Bhattacharjee, L. Hj De Haan, N. M. Evers, et al., "Role of Surface Charge and oxidative Stress in Cytotoxicity of Organic Monolayer-Coated Silicon Nanoparticles Towards Macrophage NR8383 Cells," *Particle and Fibre Toxicology* 7 (2010): 25, https://doi.org/10.1186/1743-8977-7-25.

66. P. García-Acevedo, Y. Piñeiro, J. Gallo, et al., "Unveiling Dipolar Interaction-Driven Magnetic Field Inhomogeneities in T2 MRI Contrast Agents," *Advanced Science* 13 (2025): 10356, https://doi.org/10.1002/advs.202510356.

67. V. Nandwana, S. R. Ryoo, S. Kanthala, et al., "Engineered Theranostic Magnetic Nanostructures: Role of Composition and Surface Coating on Magnetic Resonance Imaging Contrast and Thermal Activation," *ACS Applied Materials & Interfaces* 8 (2016): 6953–6961.

68. P. Cheah, T. Cowan, R. Zhang, et al., "Continuous Growth Phenomenon for Direct Synthesis of Monodisperse Water-Soluble Iron Oxide Nanoparticles with Extraordinarily High Relaxivity," *Nanoscale* 12 (2020): 9272–9283.

69. S. Tong, S. Hou, Z. Zheng, J. Zhou, and G. Bao, "Coating Optimization of Superparamagnetic Iron Oxide Nanoparticles for High T2 Relaxivity," *Nano Letters* 10 (2010): 4607–4613.

70. L. E. W. LaConte, N. Nitin, O. Zurkiya, et al., "Coating Thickness of Magnetic Iron Oxide Nanoparticles Affects R2 Relaxivity," *Journal of Magnetic Resonance Imaging* 26 (2007): 1634–1641.

71. J. Mohapatra, A. Mitra, H. Tyagi, D. Bahadur, and M. Aslam, "Iron Oxide Nanorods as High-Performance Magnetic Resonance Imaging Contrast Agents," *Nanoscale* 7 (2015): 9174–9184.

72. L. Yang, Z. Wang, L. Ma, et al., "The Roles of Morphology on the Relaxation Rates of Magnetic Nanoparticles," *ACS Nano* 12 (2018): 4605–4614.

73. J. T. Jang, H. Nah, J. H. Lee, S. H. Moon, M. G. Kim, and J. Cheon, "Critical Enhancements of MRI Contrast and Hyperthermic Effects by Dopant-Controlled Magnetic Nanoparticles," *Angewandte Chemie International Edition* 48 (2009): 1234–1238.

74. Q. L. Vuong, J. F. Berret, J. Fresnais, Y. Gossuin, and O. Sandre, "A Universal Scaling Law to Predict the Efficiency of Magnetic Nanoparticles as MRI T2-Contrast Agents," *Advanced Healthcare Materials* 1 (2012): 502–512.

75. N. Lee, Y. Choi, Y. Lee, et al., "Water-Dispersible Ferrimagnetic Iron Oxide Nanocubes with Extremely High r2 Relaxivity for Highly Sensitive in Vivo MRI of Tumors," *Nano Letters* 12 (2012): 3127–3131.

76. L. Yang, C. Sun, H. Lin, et al., "Sensitive Contrast-Enhanced Magnetic Resonance Imaging of Orthotopic and Metastatic Hepatic Tumors by Ultralow Doses of Zinc Ferrite Octapods," *Chemistry of Materials* 31 (2019): 1381–1390.

77. N. Pothayee, S. Balasubramaniam, N. Pothayee, et al., "Magnetic Nanoclusters with Hydrophilic Spacing for Dual Drug Delivery and Sensitive Magnetic Resonance Imaging," *Journal of Materials Chemistry B* 1 (2013): 1142–1149.

78. S. Chakraborty, D. Menon, V. S. Akhil Varri, et al., "Does the Doping Strategy of Ferrite Nanoparticles Create a Correlation Between Reactivity and Toxicity?," *Environmental Science: Nano* 10 (2023): 1553–1569.

79. K. Riahi, N. Sommer, A. Filatova, et al., "The Influence of the Shape of Magnetic Nanoparticles on Magnetic Hyperthermia and Cellular Internalisation," *Journal of Alloys and Compounds* 1045 (2025): 184692, https://doi.org/10.1016/j.jallcom.2025.184692.

80. J. H. Lee, J. E. Ju, B. Il Kim, et al., "Rod-Shaped Iron Oxide Nanoparticles are More Toxic Than Sphere-Shaped Nanoparticles to Murine Macrophage Cells," *Environmental Toxicology and Chemistry* 33 (2014): 2759–2766.

81. A. M. Hersh, S. Alomari, and B. M. Tyler, "Crossing the Blood-Brain Barrier: Advances in Nanoparticle Technology for Drug Delivery in Neuro-Oncology," *International Journal of Molecular Sciences* 23 (2022): 4153, https://doi.org/10.3390/ijms23084153.

82. Y. Xiao and J. Du, "Superparamagnetic Nanoparticles for Biomedical Applications," *Journal of Materials Chemistry B* 8 (2020): 354–367.

83. Y. Huang, X. Cai, Y. Li, M. Zhang, J. Sheng, and N. Gu, "The Metabolic Fate of Iron-Based Magnetic Nanomaterials and Their Impact on Macrophage Function," *Magnetic Medicine* 1 (2025): 100002.

84. J. Nowak-Jary and B. Machnicka, "In Vivo Biodistribution and Clearance of Magnetic Iron Oxide Nanoparticles for Medical Applications," *International Journal of Nanomedicine* 18 (2023): 4067–4100.

85. J. Nowak-Jary and B. Machnicka, "Comprehensive Analysis of the Potential Toxicity of Magnetic Iron Oxide Nanoparticles for Medical Applications: Cellular Mechanisms and Systemic Effects," *International Journal of Molecular Sciences* 25 (2024): 12013, https://doi.org/10.3390/ijms252212013.

86. Q. Feng, X. Xu, C. Wei, et al., "The Dynamic Interactions Between Nanoparticles and Macrophages Impact Their Fate in Brain Tumors," *Small* 17 (2021): 2103600, https://doi.org/10.1002/smll.202103600.

87. J. Gao, Q. Song, X. Gu, et al., "Intracerebral Fate of Organic and Inorganic Nanoparticles is Dependent on Microglial Extracellular Vesicle Function," *Nature Nanotechnology* 19 (2024): 376–386.

88. M. Peviani, U. Capasso Palmiero, F. Cecere, R. Milazzo, D. Moscatelli, and A. Biffi, "Biodegradable Polymeric Nanoparticles Administered in the Cerebrospinal Fluid: Brain Biodistribution, Preferential Internalization in Microglia and Implications for Cell-Selective Drug Release," *Biomaterials* 209 (2019): 25–40.

89. A. Pardo, B. Pelaz, J. Gallo, et al., "Synthesis, Characterization, and Evaluation of Superparamagnetic Doped Ferrites as Potential Therapeutic Nanotools," *Chemistry of Materials* 32 (2020): 2220–2231.

90. M. Moros, B. Pelaz, P. López-Larrubia, et al., "Engineering Biofunctional Magnetic Nanoparticles for Biotechnological Applications," *Nanoscale* 2 (2010): 1746–1755.

91. Y. Moldes-Diz, G. Eibes, C. Vázquez-Vázquez, et al., "A Novel Enzyme Catalysis Reactor Based on Superparamagnetic Nanoparticles for Biotechnological Applications," *Journal of Environmental Chemical Engineering* 6 (2018): 5950–5960.

92. P. García-Acevedo, M. A. González-Gómez, Á. Arnosa-Prieto, L. de Castro-Alves, Y. Piñeiro, and J. Rivas, "Role of Dipolar Interactions on the Determination of the Effective Magnetic Anisotropy in Iron Oxide

Nanoparticles," *Advanced Science* 10 (2023): 2203397, https://doi.org/10.1002/advs.202203397.

93. B. Argibay, J. Trekker, U. Himmelreich, et al., "Intraarterial Route Increases the Risk of Cerebral Lesions After Mesenchymal Cell Administration in Animal Model of Ischemia," *Scientific Reports* 7 (2017): 40758, https://doi.org/10.1038/srep40758.

Supporting Information

Additional supporting information can be found online in the Supporting Information section.

Supporting File: smll72478-sup-0001-SuppMat.pdf.